Modeling the Day-to-Day Variability of Midnight Equatorial Plasma Bubbles with SAMI3/WACCM-X

Min-Yang Chou[1,2], Jia Yue[1,2], Fabrizio Sassi[3], Joseph D. Huba[4], Sarah McDonald[3], Jennifer Tate[5], Nicholas Pedatella[6,7], Cora E. Randall[8,9], V. Lynn Harvey[8,9]

1. NASA Goddard Space Flight Center, Community Coordinated Modeling Center, Greenbelt, MD, USA
2. Department of Physics, Catholic University of America, Washington, DC, USA
3. Naval Research Laboratory, Space Science Division, Washington, DC, USA
4. Syntek Technologies, Fairfax, VA, USA
5. Computational Physics, Inc., Springfield, VA, USA
6. High Altitude Observatory, National Center for Atmospheric Research, Boulder, CO, USA
7. COSMIC Program Office, University Corporation for Atmospheric Research, Boulder, CO, USA
8. Laboratory for Atmospheric Space Physics, University of Colorado, Boulder, CO, USA
9. Department of Atmospheric and Oceanic Sciences, University of Colorado, Boulder, CO, USA

Key points:

1. SAMI3/WACCM-X self-consistently generates EPBs at midnight.
2. Gravity waves and meridional winds affect the spatial and longitudinal distributions of EPBs.
3. Westward winds associated with solar terminator and gravity waves facilitate the midnight EPB development by generating midnight vortex.

Abstract

It is well-known that equatorial plasma bubbles (EPBs) are highly correlated to the post-sunset rise of the ionosphere on a climatological basis. However, when proceeding to the daily EPB development, what controls the day-to-day/longitudinal variability of EPBs remains a puzzle. In this study, we investigate the underlying physics responsible for the day-to-day/longitudinal variability of EPBs using the Sami3 is A Model of the Ionosphere (SAMI3) and the Whole Atmosphere Community Climate Model with thermosphere-ionosphere eXtension (WACCM-X). Simulation results on October 20, 22, and 24, 2020 were presented. SAMI3/WACCM-X self-consistently generated midnight EPBs on October 20 and 24, displaying irregular and regular spatial distributions, respectively. However, EPBs are absent on October 22. We investigate the role of gravity waves on upwelling growth and EPB development and discuss how gravity waves contribute to the distributions of EPBs. Of particular significance is that we found the westward wind associated with solar terminator waves and gravity waves causes midnight vertical drift enhancement and collisional shear instability, which provides conditions favorable for the upwelling growth and EPB development. The converging and diverging winds associated with solar terminator waves and midnight temperature maximum also affect the longitudinal distribution of EPBs. The absence of EPBs on October 22 is related to the weak upward drift induced by weak westward wind associated with solar terminator waves.

Plain Language Summary

Plasma bubbles are a particular space weather phenomenon that mainly occurs in the nighttime equatorial region. After sunset, the bottomside ionosphere (~100-200 km) becomes unstable due to the vertical motion of the ionosphere. Bubbles can develop from the bottomside ionosphere and stretch into the topside ionosphere (above 500 km), like wax bubbles in a lava lamp. Bubbles significantly reduce the plasma density in the ionosphere, displaying turbulent plume structures that can disrupt radio wave communications and GPS navigation. Understanding and predicting the development of plasma bubbles has baffled scientists for more than 80 years, especially in understanding the day-to-day variability. In this study, we aim to understand what controls the day-to-day variability of plasma bubbles by using the physics-based SAMI3/WACCM-X model. We found that gravity waves are ubiquitous and play a vital role in seeding and determining the spacing between plasma bubbles. The longitudinal distribution of plasma bubbles is affected by meridional wind. The most striking finding is that daily dusk solar terminator waves significantly impact neutral wind and electrodynamics, controlling the presence or absence of plasma bubbles at midnight. This study reveals that the day-to-day variability of plasma bubbles is considerably linked to the variations of the lower atmosphere.

1. Introduction

Equatorial spread F (ESF) and equatorial plasma bubbles (EPBs) are ionosphere irregularities that primarily occur in the nighttime equatorial ionosphere. Brook and Wells (1938) first observed spread echoes from the ionospheric F region, referred to as ESF, using ionosondes. Woodman and LaHoz (1976) proposed the concept of ionospheric "bubbles" to illustrate the nonlinear evolution of plasma depletions from the bottom to the topside ionosphere. EPBs are field-aligned structures in the form of meridionally-elongated wedges of plasma depletions in both hemispheres (e.g., Kil et al., 2009), which are characterized by bite-outs in ion density measurements (Heelis et al., 2010; Yokoyama et al., 2011), plume structures in radar observations (Kelley et al., 1981; Hysell et al., 2009), intensity depletions in airglow images (e.g., Kelley et al., 2003; Otsuka et al., 2002; Eastes et al., 2019; Chou et al., 2020a), and turbulent fluctuations in Global Navigation Satellite System Total Electron Content (TEC)(Nishioka et al., 2008; Cherniak and Zakharenkova, 2016). Understanding and forecasting the presence of EPBs is an essential topic since they can disrupt propagation of radio waves used in global communication and navigation systems (e.g., Kelley et al., 2014; Xiong et al., 2016) and cause scintillations in radio signals (e.g., Yeh and Liu, 1982; Kintner et al., 2007).

Tsunoda (1985) first proposed the longitudinal and seasonal distribution of EPBs is related to the angle between dusk solar terminator and geomagnetic field line at the magnetic equator. The pre-reversal enhancement (PRE) of upward E×B drift occurs when the dusk solar terminator is aligned with the geomagnetic field line, resulting in the post-sunset rise (PSSR) of ionosphere. The PSSR destabilizes the ionosphere and allows EPBs to develop through the Rayleigh-Taylor (RT) instability (Sultan et al., 1996). The PSSR-to-EPB paradigm (Tsunoda et al., 2018) is supported by satellite observations that the PRE controls the EPB occurrence on a climatological basis (Burke et al., 2004; Gentile et al., 2006; Huang and Hairston, 2015).

However, PRE fails to explain the occurrence of EPBs on a day-to-day basis. EPB development during the post-midnight have been observed by the Formosa satellite-1 (FORMOSAT-1 or ROCSAT-1), Communication/Navigation Outage Forecasting System (C/NOFS), and radar observations (e.g., Yizengaw et al., 2000; Yokoyama et al., 2011; Nishioka et a., 2012). Tsunoda (2015) further proposed an upwelling paradigm to describe the processes of EPB development from seeding, upwelling growth, and EPB formation. Upwelling (local uplift of the bottomside ionosphere) or large-scale wave structure (LSWS, a continuous distribution of upwellings) is the undulation of the bottomside ionosphere, mainly driven by an eastward polarization electric field (Ep). Tsunoda et al. (2018) suggested that the amplification of upwelling (i.e., upwelling growth) is comparable to the post-sunset rise (PSSR) of the ionosphere and can make an additive localized uplift to the PSSR by ~50 km (e.g., Chou et al., 2020a), leading to the conclusion that upwelling growth controls the EPB

development, instead of PRE. The source of upwelling remains a mystery; however, seed perturbations related to gravity waves are considered to be the most credible source of upwellings (e.g., Tulasi Ram et al., 2014; Chou et al., 2020a; Huba and Liu, 2020).

Understanding the complexities of the underlying physics responsible for day-to-day variability of EPBs remains a challenge. Various observation and modeling efforts have been conducted to investigate underlying physics responsible for the day-to-day variability of EPBs, such as seed perturbations (Singh et al., 1997; Abdu et al., 2009; Retterer et al., 2014; Krall et al., 2013), neutral winds (Maruyama and Matuura, 1984; Huba et al., 2009; Krall et al., 2009, 2021; Huba and Krall, 2013), vertical drifts (Retterer et al., 2005; Su et al., 2009), shear instability (Hysell and Kudeki, 2004; Yokoyama et al., 2015), Es-layer instability (Tsunoda, 2007; Huba et al., 2020), tidal forcing (Tsunoda et al., 2015; Chang et al., 2020; Chou et al., 2020b), upwelling growth (e.g., Tsunoda, 2015), and penetration electric fields due to geomagnetic storms (e.g., Cherniak and Zakharenkova, 2016; Rajesh et al., 2017). These studies primarily focus on a single driver that controls EPB development, and artificial seed perturbations are required in the initial conditions for EPB simulations (e.g., Yokoyama, 2017). However, the onset of EPBs could concurrently involve multiple drivers and physical processes. Limited observational instruments and modeling capability prohibit a complete understanding of the complex physical processes of EPB onset. Therefore, comprehensive observations and coupled whole atmosphere/ionosphere models that consider more realistic background conditions and include all drivers (e.g., Huba and Liu, 2020; Hysell et al., 2022), are necessary to provide the whole picture for comprehending the morphology and day-to-day variability of EPBs.

Recent advances in satellite measurement techniques and modeling capabilities have enabled improved understanding of the complex processes that cause day-to-day variability of EPBs. The National Aeronautics and Space Administration (NASA) Global-scale Observations of the Limb and Disk (GOLD) mission has provided unprecedented daily observations of equatorial ionization anomaly (EIA) images from western Africa to South America. Eastes et al. (2019) reported that GOLD observed EPBs on most nights, displaying significant spatial and temporal variability that is unexpected during solar minimum conditions. Huba and Liu (2020) further conducted a high-resolution global simulation of EPBs using the Sami3 is A Model of the Ionosphere (SAMI3) and the high-resolution Whole Atmosphere Community Climate Model with thermosphere-ionosphere eXtension (WACCM-X). The coupled SAMI3/WACCM-X self-consistently generated EPBs for the first time, comparable to the GOLD observations (Eastes et al., 2019). They found that EPBs developed for a March case but not for a July case, which agrees well with the observations (e.g., Gentile et al., 2006). Huba and Liu (2020) suggested that gravity waves play an essential role in seeding EPBs because EPBs are absent when SAMI3 is coupled to empirical models, such as HWM and MSIS.

However, many questions remain unsolved with regard to EPBs: What is the linkage between gravity waves and upwellings? What is the most crucial factor that controls upwelling growth (e.g., Tsunoda, 2015)? What influences the spacing between EPBs and the longitudinal distribution of EPBs? Why do EPBs show isolated clusters separated by long distances on some nights but display a continuous distribution of EPB trains on other nights? Why do EPBs occur on some nights and not on others? What is the physics responsible for the EPBs occurred during midnight without PRE (e.g., Otsuka, 2018)? What is the underlying mechanism for generating large-scale EPBs (e.g., Eastes et al., 2019)?

In this study, the coupled SAMI3/WACCM-X model is utilized to investigate the day-to-day variability of EPBs. Simulation on October 20, 22, and 24 in 2020, during a solar minimum period, is presented. EPBs are generated on October 20 and 24 at midnight, but not on October 22. EPBs display irregular and regular spatial distributions on October 20 and 24, respectively. The underlying mechanisms and background conditions that cause the absence and presence of the midnight EPBs, as well as the spatial distribution are discussed. We outline the effects of gravity waves and neutral winds on the longitudinal distribution of EPBs and elucidate how solar terminator waves affect the ionospheric electrodynamics and facilitate the midnight EPB development. This study affords new insight into the day-to-day variability of EPBs during solar minimum.

2. SAMI3/WACCM-X

In this work we performed simulations using the SAMI3 model driven by WACCM-X (McDonald et al., 2015). SAMI3 is a global, three-dimensional, physics-based ionosphere model. It is based on the two-dimensional SAMI2 model (Huba et al., 2000). SAMI3 models the plasma and chemical evolution of seven ion species (H^+, He^+, N^+, O^+, N_2^+, NO^+, and O_2^+) and solves the ion continuity and momentum equations for seven ion species. Ion inertia is included in the ion momentum equation for motion along the geomagnetic field. The electric fields driven by the neutral wind dynamo are self-consistently solved from the potential equation based on current conservation ($\nabla \cdot J = 0$) and equipotential field lines (e.g., Huba et al., 2008). The model also solves the complete temperature equations for electrons and three ion species (H^+, He^+, and O^+). SAMI3 uses the solar EUV irradiance model for aeronomic calculations (EUVAC). The Richmond Apex model (Richmond, 1995) is used to specify the magnetic field (i.e., International Geomagnetic Reference Field, IGRF). The thermospheric inputs of neutral composition, temperature and winds can be specified in SAMI3 by analytical models, empirical models (e.g., HWM and MSIS), or physics-based models (e.g., Huba et al., 2010, 2017).

In this study, the thermospheric variables (neutral densities, winds, and temperatures) from WACCM-X are inputs into SAMI3 (e.g., McDonald et al., 2015, 2018). A detailed description of WACCM-X is given in Liu et al. (2018). The WACCM-X resolution is

0.47°×0.625° in latitude and longitude. The upper boundary of WACCM-X is at 4×10^{-10} hPa (approximately 450 km on average). SAMI3 uses a geomagnetic grid of dimension (nz, nf, nl) = (160,160,194), where nz is the number of grid points along the magnetic field line, nf is the number of field lines, and nl is the number of magnetic longitudes. SAMI3 used a non-uniform longitudinal grid in this study, including coarse- and high-resolution regions (e.g., Huba et al., 2010). The longitudinal resolution is 0.6° from ~63.6°-136.5°W and 4° at the other longitudes. The latitudinal resolution is variable due to the nonlinear spacing of grid points along field lines. The resolution is approximately 0.2° near the magnetic equator and 0.66° at 40° latitude at ~300 km altitude. Simulation on October 20, 22, and 24 in 2020 is performed using the following geophysical conditions: F10.7=74, 74.2, 71.3; F10.7A=78.2, 79, 79.8; Ap = 4, 5, 17; Kp = 1, 1, 3. EPBs develop in the high-resolution region; thus, we focus on the region from ~63.6°-136.5°W.

3. Results and Discussions

3.1 Day-to-Day variability of EPBs

Figure 1 shows the TEC simulated from SAMI3/WACCM-X at 08:00 UT, 08:00 UT, and 10:00 UT on 20, 22, and 24 October 2020, respectively. Note that different UT times are presented for each day due to the difference in EPB onset time. Distinct TEC depletions associated with EPBs are discernible in the equatorial ionosphere on October 20 and 24 but not on October 22. EPBs display irregular spatial distribution with two groups of EPBs on October 20. On October 20, the first group shows two isolated small-scale EPBs from 105°W-120°W, and the other shows one large-scale EPB around 90°W over the Pacific Ocean. These EPBs developed around the local midnight. There are no EPBs on October 22, but a regular spatial distribution of successive post-midnight EPBs occurred on October 24. Approximately eight clusters of EPBs spanning ~75° in longitude can be discerned.

Of particular interest is the mechanism that causes regular and irregular spatial distributions of EPBs. Both irregular and regular spatial distributions of EPBs are commonly observed by satellite observations such as the C/NOFS and GOLD (e.g., Huang et al., 2013; Eastes et al., 2019). Makela et al. (2010) suggested that gravity waves in the bottomside ionosphere play a vital role in the quasi-periodically spaced EPBs (Figure 1c); however, the underlying mechanism responsible for the long-distance separation of the EPB groups (Figure 1a) remains unknown. Additionally, Figure 1a shows a large-scale EPB near the west coast of South America. Eastes et al. (2019) first identified the large-scale EPB with significant deviations in separation of the EIA crests compared to the adjacent longitudes. They suggested that penetration electric fields due to negative excursion in the interplanetary magnetic field Bz may be responsible for the abrupt shifts of EIA. Nevertheless, the exact mechanism responsible for the large-scale EPBs remains unknown.

3.2 Gravity Wave Seeding and Upwelling growth

Tsunoda et al. (2018) suggested that upwelling growth controls the EPB development and gravity waves appear to be the most credible source of upwellings (e.g., Tulasi Ram et al., 2014; Chou et al., 2020a). To investigate the linkage between gravity waves and upwellings, Figure 2 shows the electron density (top panels) and zonal wind perturbations (bottom panels) as a function of longitude and altitude on 20, 22, and 24 October. Wu et al. (2015) suggested that zonal and vertical wind perturbations associated with gravity waves were most effective in seeding EPBs because the zonal and vertical winds can effectively modify the electrostatic potential. Thus, we extract the zonal wind perturbations by applying a fifth-order high-pass filter with a cutoff period of 45 min, which covers typical period ranges for gravity waves from various sources in the upper atmosphere and ionosphere (e.g., Azeem et al., 2015; Chou et al., 2017; Sharon and Azeem, 2021; Heale et al., 2022; Yue et al., 2022).

Multiple instances of upwelling (indicated by black arrows) can be identified in the iso-density contours of ~$10^{3.5}$ cm^{-3} along the bottomside ionosphere before the EPB development at ~07:05 UT and 07:00 UT on 20 and 24 October (Figures 2a and 2c). These upwelling structures are identical to the incoherent scatter radar observations (see Figure 1 of Tsunoda et al, 2018). The zonal scales of upwellings are also consistent with previous observations of ~100-1500 km (Tsunoda, 2021). EPBs eventually developed from the crests of upwellings as shown in Figure 1. On the other hand, Figure 2b shows no evidence of upwellings; this is due to the lower bottomside ionospheric layer height of ~150-200 km (iso-density contour of ~$10^{3.5}$ cm^{-3}, or peak density height (hmF2) ~250-300 km) on this night compared with Figures 2a and 2c (above ~300 km in iso-density contour of ~$10^{3.5}$ cm^{-3}, or hmF2~350-400 km). EPBs tend to develop when hmF2 is around 350-400 km, generally consistent with the FORMOSAT-3/COSMIC observations (e.g., Chou et al., 2020b). Note large-scale EPB and fossil EPB are presented at ~90°W and ~65°W, respectively, in Figure 2a. Two upwellings within the longitude range of 75-90°W in Figure 2a do not lead to EPB development because the lower ionosphere height inhibits the upwelling growth.

The bottom panels of Figure 2 are the zonal wind perturbations extracted by a high-pass filter, which can be attributed to gravity waves in the WACCM-X model (Liu et al., 2014). Gravity wave seeding is important for EPB development (Huba and Liu, 2020). We found that the zonal scales of upwellings and zonal wind perturbations are generally comparable. This reveals that the zonal scale of gravity waves plays a vital role in determining the spacing between EPBs. However, gravity waves alone are insufficient for upwelling growth (Figure 2b); a sufficiently high ionospheric layer is essential to facilitate the upwelling growth since the lower ionospheric layer height results in higher ion-neutral collision frequency and smaller growth rate (e.g., Saito and Maruyama, 2007). This also explains why upwellings tend to be amplified during the PSSR (Tsunoda, 2015). The physical mechanisms responsible for the ionospheric layer height variation will be discussed in the next section.

Note that the upwellings do not necessarily correspond to the specific phase front of gravity waves since the upwellings are stationary, but gravity waves are not. Upwellings are developed via Ep×B drift (e.g., Tsunoda, 2015). The various zonal scales of gravity waves also partly explain why the EPBs occur in isolated regions on some nights (Figure 1a), but on other nights EPBs display a quasiperiodic wave-train, extending over thousands of kilometers in the zonal distance (Figure 1c).

There are two scenarios that could explain the interplay between gravity waves and upwellings. The first scenario is under ideal background conditions (e.g., solar maximum, equinoxes, strong upward drift, higher ionospheric layer height), when weak gravity wave perturbation is sufficient for the upwelling growth as shown in Figures 2a and 2c due to higher bottomside ionospheric layer height (i.e., large growth rate). The passage of gravity waves causes bottomside ionospheric undulations through ion-neutral coupling processes, leading to inhomogeneity of the Pedersen conductivity. A divergent charge would pile up on the edges of seed perturbations when eastward Pedersen current driven by gravity or equatorward neutral winds flow over this region, setting up polarization electric fields (Ep) to satisfy ionospheric current-free conditions ($\nabla \cdot J = 0$). Upwelling or LSWS eventually develop in the bottomside ionosphere via Ep×B drifts.

The other scenario is when the background condition does not favor the upwelling growth (e.g., solar minimum, solstices, weak upward drift, lower ionospheric layer height), so strong gravity wave perturbations in the neutral wind become critical (e.g., Aa et al., 2022; Rajesh et al., 2022; Harding et al., 2022). Vertical oscillations of gravity wave-driven neutral winds can drive zonal divergent Pedersen currents (J~=U×B) and Ep should be established to cancel the Pedersen currents, leading to upwelling growth (e.g., Eccles, 2004; Tsunoda, 2010; 2021).

In Figure 3, we examine temperature perturbations from WACCM-X as a function of longitude and latitude at ~350 km on 20, 22, and 24 October to confirm the presence and morphology of gravity waves. The morphology of wave patterns is quite complicated, likely due to the interference of gravity waves from different sources. We found that gravity waves are ubiquitous and could act as natural seeds for the formation of upwelling, albeit there are enhanced perturbations at mid-latitudes that may be related to mountain waves or convectively-generated gravity waves (cf. Ern et al., 2011). There are many sources that could generate gravity waves, such as deep convection (e.g., Yue et al., 2009), solar terminator waves (Bespalova et al., 2016), and oceanic waves (Zobotin et al., 2016). However, more careful studies of these gravity waves are out of scope for this paper. Future work will focus on analyzing the wave sources related to EPB development.

Of particular significance is that Figure 3a shows distinct southwestward propagating planar gravity waves at the magnetic equator from 105°-120°W. The large-scale zonal wind perturbations shown in Figure 2d are therefore related to the planar gravity waves. Tsunoda

(2010, 2013) and Krall et al. (2013) suggested that planar gravity waves cannot seed EPBs effectively because the coupling of planar gravity waves to the ionosphere tends to be weak when the wave phase fronts are not aligned with geomagnetic field lines. Thus, the alternating contributions of upward and downward winds to the electric potential cancel each other out along the same field line. In Figures 3b and 3c, multiple concentric waves can be identified near the magnetic equator. Tsunoda (2010) suggested that concentric gravity waves can seed EPBs effectively because the polarization response is more efficient when the wavefront is aligned with the geomagnetic field lines. The discrepancy of planar and concentric gravity waves could partly explain the longitudinal distribution of EPBs shown in Figures 1a and 1c. The zonal scale and wavefront orientation of gravity waves therefore control the spacing between EPBs.

3.3 Electric Field and Neutral Wind Effects

Gravity wave seeding is crucial for the formation of upwellings, but sufficient ionospheric layer height is necessary to facilitate upwelling growth and EPB development. In the nighttime topical ionosphere, the F region plasma dynamics are governed by a complex interplay between motions of electromagnetic forces, neutral winds, gravity, and pressure gradient (Kelley, 2009). The equilibrium of the ionosphere is primarily affected by neutral wind, gravitational and electromagnetic forces since the pressure gradient term produces negligible effects in the global electrodynamics (Perkins, 1973; Eccles, 2004; Maute et al., 2012). To understand the background conditions responsible for the day-to-day variability of EPBs, we examine the effects of E×B drift and neutral wind on the ionospheric layer height variation. In this section, we will first discuss the background conditions related to the irregular spatial distribution of EPBs on October 20. Then, we will discuss the absence and regular spatial distribution of EPBs on October 22 and 24, respectively; both cases show similar initial background conditions at 05:00 UT.

3.3.1 Irregular Spatial Distribution of EPBs on October 20

Figure 4 shows the time sequence of electron density (top panels), vertical E×B drift (middle panels), and zonal E×B drift (bottom panels) as a function of longitude (local time) and altitude on October 20. An EPB that occurred after sunset is discernible from 60°-75°W due to strong PRE vertical drifts after 00:00 UT. Here we focus on the EPBs that developed after 0500 UT. The PRE-related upward E×B drift enhancement is visible around 100°-135°W below ~600 km altitude (Figure 4f). EPBs do not develop following the PRE because of the weak upward E×B drifts (~20 m/s) and lower bottomside ionospheric layer heights (below 300 km). However, significant localized upward E×B drift enhancements of ~20-50 m/s occurred around 80-120°W in the topside ionosphere (700-1000 km) after 0500 UT. The localized upward E×B drifts further moved downward and westward and made an additive

contribution to the PRE vertical drifts, raising the ionosphere to higher altitudes of ~350 km (Figure 4c) and contributing to the upwelling growth and large-scale EPB development at ~90°W at 0530 UT.

The localized upward E×B drift enhancement causes significant undulations of the ionospheric layer height, resulting in large zonal and vertical plasma density gradients. Under such conditions, the large-scale gravity-driven Pedersen current becomes important in equatorial ionospheric electrodynamics (Eccles, 2004; Maus and Luhr, 2006; Burke et al., 2009). Eccles (2004) suggested that gravity-driven current is an essential source of large-scale Ep (λ > 1000 km) during the nighttime ionosphere. As the eastward gravity-driven Pedersen current flows over the undulating bottomside ionosphere, Ep will develop and lead to more prominent ionospheric undulations through Ep×B drifts. In our opinion, this explains the alternating large-scale upward and downward drifts in Figure 4 after 0500 UT. The presence of large-scale upward E×B drifts further leads to the development of upwellings in the bottomside ionosphere near midnight with small-scale upward E×B drifts of ~30-50 m/s (Figures 4d and 4i), which are superimposed on the large-scale upward E×B drifts. We can identify two upwellings that developed around 110°-120°W at 07:00 UT and EPBs that developed from the crests of the upwellings after midnight. At 08:00 UT, more pronounced ionospheric undulations occur because of the contribution of gravity-driven eastward Pedersen current around 90-110°W (Figures 4e and 4j). Such large ionospheric undulations extending over ~200-300 km in altitude have been observed by Jicamarca radar (Kelley et al., 1981). The dynamic vertical E×B drifts significantly affect the longitudinal variation of ionospheric layer height and the longitudinal distribution of EPBs. The distribution of large-scale upward E×B drifts also explains why the EPBs are confined within ~85°-120°W.

An additional simulation excluding the gravity-driven current terms in the potential equation (Huba and Joyce, 2010) has been conducted. The gravity-driven electric current can contribute additional large-scale vertical E×B drifts of ~10-20 m/s during the nighttime (not shown), consistent with the previous simulations and observations (e.g., Eccles, 2004; Stoneback et al., 2011). Such midnight upward drift enhancements have been observed by FORMOSAT-1 and C/NOFS during quiet time conditions (e.g., Yizengaw et al., 2009; Heelis et al., 2010; Stoneback et al., 2011).

The bottom panels of Figure 4 show that the corresponding zonal E×B drifts display strong vertical shear flow with plasma moving eastward at up to ~150 m/s above 300 km and westward at up to ~150 m/s below 300 km, consistent with the NASA sounding rocket experiments during the postsunset equatorial ionosphere (Hysell et al., 2005). We noticed that clear localized retrograde flow (westward E×B drifts) embedded within the F region eastward plasma flow emerged in the topside ionosphere at 05:00 UT (Figure 4k), and the movement of the retrograde flow is accompanied by the localized upward E×B drift enhancement (Figures 4f and 4g). The retrograde flow keeps moving westward and

downward, eventually encountering the westward flow below 300 km at 06:00 UT, which in turn elevates the westward flow to a higher altitude of ~400 km, destabilizing the bottomside ionosphere and resulting in shear instability (Figures 4m and 4n). The shear flow accompanies the upward and downward E×B drifts between 60°W and 105°W, displaying a midnight equatorial vortex feature that is commonly observed in the post-sunset periods (e.g., Kudeki and Bhattacharyya, 1999; Lee et al., 2014). These processes allow upwelling growth and EPB development, supporting the hypothesis proposed by Hysell and Kudeki (2004) that the shear instability could precondition the ionosphere for the RT instability. Considering that the nighttime eastward plasma flow in the F region is related to the eastward wind (cf. Heelis, 2004), the retrograde flow could be related to the F region westward wind. To confirm this hypothesis, we further examine neutral winds since they affect the ionospheric layer height and electrodynamics (e.g., Heelis, 2004; Lin et al., 2007).

Figure 5 shows the time sequence of meridional (top) and zonal (bottom) winds at ~460 km on October 20. The cross-equatorial meridional winds are mainly northward around ~75°-120°W over the magnetic equator at 05:00 UT. However, we note that the meridional winds display distinct band structures with alternating wind directions. The wind patterns tend to move southwestward, extending from northwest to southeast. The meridional winds between ~95°-135°W in the northern hemisphere are mainly northward at 05:00 UT and gradually turn southward, leading to a converging wind pattern between ~90°-135°W over the magnetic equator at ~06:00 UT. Converging winds can facilitate the RT instability because the converging winds can raise the ionosphere to higher altitude along the field line, leading to a decrease of integrated Pedersen conductivity and ion-neutral collision frequency (Huba and Krall, 2013). The downward component of converging winds is also an additive driver for the RT instability (Tsunoda, 2021) because the downward wind can drive eastward Pedersen current contributing to the RT instability, similar to the gravity-driven eastward electric current.

We note that the meridional winds gradually turn to a poleward direction between 60°-90°W after 05:00 UT (after 24:00 LT at 75°W), exhibiting a typical midnight temperature maximum (MTM) wind pattern over the magnetic equator (c.f., Fang et al., 2016). The occurrence of MTM could result in localized reversal of the large-scale eastward and equatorial winds during the nighttime. This can be seen in Figures 5f-j, in that the eastward zonal wind over the MTM slows down and reverses to westward. The poleward winds further lower the ionosphere and weaken RT instability between ~60°-90°W (cf., Huba and Krall, 2013). The downward motion of the ionosphere from 60°-90°W is, therefore, due to the combined effects of the southward wind, downward E×B drifts, and MTM winds. The distribution of meridional winds generally reflects the longitudinal variation of ionospheric layer height (top panel of Figure 4), demonstrating that the meridional wind is another important factor in determining the longitudinal distribution of EPBs.

Of particular significance is that the meridional winds display a blue narrow band structure (southward wind) accompanying with large-scale northward winds extending from northwest to southeast in the northern hemisphere, which appears to be related to the planar gravity waves (Figure 3a) and solar terminator waves. We will discuss the large-scale solar terminator waves in section 3.4. The narrow band wind structure also can be identified in the zonal wind, in that the presence of a westward wind causes cessation of the eastward wind. Compared with the vertical and zonal E×B drifts (Figure 4), the retrograde flow and upward E×B drift enhancement in the equatorial F region can be attributed to this narrow band wind structure since the orientation of retrograde flow is consistent with the narrow band wind structure. Since the neutral wind perturbations can result in inhomogeneous electric conductivity distribution, the divergence and convergence of zonal wind driven dynamo currents cause accumulation of electric charges. The westward winds play a vital role on the development of retrograde flow and upward E×B drift over the magnetic equator by generating Ep mapping to the magnetic equator, contrary to the post-sunset ionospheric conditions where the vertical drift is primarily driven by the eastward acceleration of zonal wind (Richmond et al., 2015).

Moreover, westward tilting eastward E×B drift enhancements are also visible on either side of the retrograde flow, which could be modulated by the downward Ep generated by eastward winds at higher latitudes. Varney et al. (2009) observed the streak patterns in zonal and vertical E×B drifts related to gravity waves in Jicamarca ion drift observations. This demonstrates that gravity waves can be the another source to drive midnight vertical drift and shear flow instability. Miller et al. (2009) reported the seeding of EPBs by the mid-latitude MSTIDs. They found that the Ep embedded within the MSTIDs can be mapped to the magnetic equator along the magnetic field lines (e.g., Chou et al., 2021) and lead to the post-midnight EPB development. Their MSTIDs displayed distinct westward-tilted band structures when the airglow images were projected to the Apex coordinate. Significant westward plasma flows embedded within the MSTIDs were also identified, consistent with our simulations.

3.3.2 Absence of EPBs on October 22

Figure 6 is the same as Figure 4, but for October 22. The PRE is small or absent near dusk due to weak eastward wind. The vertical E×B drift generally shows typical downward drift throughout the night (e.g., Scherliess and Fejer, 1999), resulting in lower ionospheric layer heights. At 05:00-07:00 UT, there are gentle large-scale bottomside ionospheric undulations accompanied by nearly zero vertical drift above the crests of upwellings due to the cancellation of small-scale upward drifts and large-scale downward drifts (Figures 6f and 6g). Significant downward drifts above the downwelling are also visible from 60°-90°W. Similar patterns of decreasing and increasing zonal E×B drifts can also be identified from

75°-90°W (Figures 6k and 6i), most likely due to the zonal wind variations. The cessation of eastward E×B drifts due to the westward-tilted retrograde flow in the F region can also be identified, and the corresponding upward E×B drifts are weak as well. After 07:00 UT, there are significant westward E×B drifts around 60°-105°W; however, the westward flow is accompanied by downward E×B drifts.

Figure 7 shows the corresponding meridional and zonal wind variations on October 22. The meridional wind also displays distinct band structures, although wind velocities are weaker than in Figure 5. Weak converging winds are not able to push the ionosphere to sufficient altitude. A blue narrow band structure (southward wind) extends from northwest to southeast in the northern hemisphere (top panels). The narrow band wind structure can also be identified in the zonal wind around 75°-120°W in the northern hemisphere at 05:00-06:00 UT (bottom panels), which is responsible for the west-tilted retrograde flow and upward E×B drifts in Figure 6. After 06:00 UT, the westward winds around 60°W in the southern hemisphere correspond to the large-scale westward plasma flow (bottom panels of Figure 6). Although the westward winds also display northwest to southeast alignment, the westward winds in the southern hemisphere can induce northward and downward Pedersen currents. Southward and westward Ep would be set up to drive westward and downward Ep×B drifts, resulting in descending ionospheric layers. Together these processes explain the absence of EPBs on October 22.

3.3.3 Regular Spatial Distribution of EPBs on October 24

Figure 8 is the same as Figure 6, but for October 24. The PRE is also weak and no EPBs develop during the post-sunset period. At ~05:00 UT, Figure 8a shows that the ionospheric layer heights are comparable with the layer heights on October 22, the no-EPB case. However, large-scale upward drifts develop near midnight and extend from ~60°W to ~135°W (Figure 8f), uplifting the bottomside ionospheric layer by at least 50 km. We found that the large-scale upward E×B drifts tilted westward at 05:00 UT, consistent with the morphology of westward retrograde flow in the F region (Figure 8k). At 06:00 UT, the retrograde flow in the F region merges with the westward E×B drifts in the bottomside ionosphere, leading to shear instability and equatorial vortex features, consistent with the October 20 case. Two upwellings are further developed around 70°-80°W at 06:00 UT (Figure 8b). The large-scale upward E×B drifts continue moving westward and lifting the ionosphere to ~300 km, leading to successive upwelling growth and EPB development.

Figure 9 shows that the meridional winds on October 24 have similar wind patterns and velocities compared with the meridional winds on October 22. However, zonal wind disparities exist, as discussed in more detail here. Much stronger westward winds can be identified over the magnetic equator during 05:00-07:00 UT on October 24 (Figures 9f-9h). Such westward winds are responsible for the retrograde flow and upward E×B drift

enhancement in Figure 8, demonstrating that the zonal wind differences are the primary reason for the absence of EPBs on one day and the presence of EPBs on the other day.

3.3.4 Mapping of Electric Fields Induced by Neutral Wind Perturbations

The most striking discovery is that the neutral wind perturbations driven by solar terminator waves and gravity waves contribute to the midnight vertical drift enhancement and collisional shear instability, as discussed in section 3.3.1-3.3.3. To investigate the linkage between neutral wind perturbations, upward E×B drift enhancement, and retrograde flow, Figure 10 shows the zonal (top panels) and vertical/meridional (bottom panels) E×B drifts as a function of latitude and altitude at ~05:00 UT along the magnetic longitudes of 337.65°, 346.05°, and 357.45° (~95.3°W, ~86.86°W and ~75.25°W in the geographic coordinate at the magnetic equator) on October 20, 22, and 24, respectively. Significant cessation of eastward E×B drift and westward E×B drift related to retrograde flows (indicated by black arrows) can be identified along the field lines, accompanying with the upward E×B drift enhancement, on October 20 and 24, respectively. However, the retrograde flow and upward E×B drift are obscure on October 22. The retrograde flows extend from ~10°N and ~5°N to the southern hemisphere on October 20 and 24, consistent with the locations of blue narrow band structures of neutral winds discussed in previous sections. This reveals that the solar terminator waves and gravity waves are responsible for the retrograde flow and midnight vertical drift enhancement. Thus, the altitudinal variation in equatorial F region plasma motion is a direct mapping of the latitudinal variation of Ep generated by solar terminator wave and gravity wave induced neutral wind perturbations (e.g., Huba et al., 2015; Chou et al., 2022; Lin et al., 2022).

As opposed to the post-sunset ionosphere, the midnight upward E×B drifts are attributed to the westward winds associated with the solar terminator waves and large-scale gravity-driven currents (e.g., Eccles., 2004). Figure 11 illustrates the mechanism of westward wind on the midnight upward E×B drift and retrograde flow. The westward winds with northwest to southeast band structure at higher latitudes can drive southward Pedersen current ($Jp \sim = U \times B$), setting up northward Ep. Due to the specific wavefront alignment of the westward wind, the eastward component of Ep can also be established. Both northward and eastward Ep will map along field lines to the magnetic equator due to high electrical conductivity of the field line, leading to westward and upward Ep×B drifts in the topside equatorial ionosphere. Gravitational force further amplifies the Ep by generating eastward Pedersen current. The westward and upward Ep×B drifts result in retrograde flow and midnight vertical drift enhancement. As the band structure of the westward wind moves southwestward, the retrograde flow moves downward and westward and merges with the westward plasma flow in the bottomside ionosphere, leading to collisional shear instability. Hysell and Kudeki (2004) and Hysell et al. (2005) suggested that the shear instability may destabilize the

bottomside ionosphere and generate precursor seed waves responsible for the EPB development. Our simulations suggest that the shear instability could be influenced by the retrograde flow associated with solar terminator wave or gravity waves. Additionally, Coley et al. (2014) showed westward plasma flow in the topside ionosphere after midnight during solar minimum. Forbes et al. (2008) also suggested that solar terminator waves are more prominent during solar minimum, implying that the westward plasma flow observed by Coley et al. (2014) may be related to solar terminator waves or gravity waves.

However, this scenario is only valid in the northern hemisphere. As the band structure of the westward wind moves to the southern hemisphere, the westward wind would induce downward E×B drift, as shown in Figures 6 and 7, due to the direction of magnetic field. Under such condition, the eastward wind with the same wavefront orientation in the southern hemisphere could induce downward and eastward Ep mapping to the magnetic equator. This demonstrates that zero or weak zonal Ep×B drift may occur due to the cancellation of vertical Ep; however, the upward Ep×B drift should persist.

Figure 12 summarizes the coupled physical processes contributing to the midnight EPB development. Neutral wind perturbations associated with gravity waves and solar terminator waves destabilize the ionosphere by generating the midnight vertical drift enhancement and shear flow instability, resulting in the midnight vortex. The midnight vortex is therefore related to gravity waves or solar terminator waves, which is different from the post-sunset vortex associated with the PRE (e.g., Tsunoda et al., 1981). The midnight vertical drift enhancement and converging winds associated with solar terminator waves further uplift the ionosphere, and gravity waves seed upwellings. The zonal scale of gravity waves determines the spacing between upwellings (or EPBs). Ep developed within upwellings further leads to upwelling growth via Ep×B drift and EPB development. The study reveals that gravity waves can not only contribute to seeding but create ionospheric conditions resembling the post-sunset ionosphere to facilitate EPB development.

3.4 Influences of Solar Terminator Waves on the Midnight EPB Development

In section 3.3, we demonstrated that the nighttime neutral wind displays distinct band structures with alternating wind directions. The converging winds and wind dynamo effect contribute to the midnight EPB development by lifting the ionosphere to higher altitude, providing conditions favorable for upwelling growth. Since the dayside solar heating and pressure bulge cannot explain the alternating wind patterns on the nightside, we propose that solar terminator waves could be the primary mechanism to explain the alternating band structures in neutral winds.

Figure 13 shows the global distribution of meridional winds at ~460 km altitude on 20, 22, and 24 October. The nighttime meridional winds (shaded area) display large-scale wind perturbations with northwest to southeast alignment (indicated by dashed lines) after the dusk

561 solar terminator and southwest to northeast alignment before the dawn solar terminator,
562 consistent with the solstice solar terminator waves in thermosphere winds and densities
563 observed by the CHAMP satellite (Forbes et al., 2008; Liu et al., 2009). These large-scale
564 wind patterns move westward with the solar terminator and can be identified daily, despite
565 the morphology and amplitude being slightly different. Medium-scale meridional wind
566 perturbations following the dusk terminator can also be identified over the continent of
567 Eurasia, which could cause post-sunrise ionospheric perturbations (e.g., Zhang et al., 2021).
568 It should be mentioned that the blue narrow band structures (southward wind) indicated by
569 white dashed lines have smaller horizontal wavelength (~10° in latitude) on October 20
570 compared with other days (~20° in latitude), which could be due to the modulation of planar
571 gravity waves shown in Figure 3a.
572 Huang et al. (2014) showed significant longitudinal asymmetry of midnight EPBs around
573 60°-150°W in October-January. This could be because the wavefront orientation of solar
574 terminator waves is aligned with the inclination angle of the magnetic equator in this region.
575 The resulting converging winds and zonal wind dynamo can lift the ionosphere to a higher
576 altitude, providing conditions favorable for EPB development. We could expect that the solar
577 terminator waves with southwest to northeast wavefront alignment near June solstice could
578 also contribute to the high occurrence of midnight EPBs around 20°-70°W near June solstice
579 (Gentile et al., 2011; Yizengaw et al., 2013).
580 On the other hand, the solar terminator waves on October 20 show more dynamic
581 features. Miyoshi et al. (2009) suggested that the solar terminator wave is mainly generated
582 by the superposition of the upward propagating migrating tides, which could contribute to the
583 generation of MTM as shown in Figure 5. The MTM winds considerably impact EPB
584 development (Krall et al., 2021) and its longitudinal distribution. McDonald et al. (2015)
585 indicated that the nonmigrating tides play an important role in the nighttime ion upward drift.
586 Tidal forcing contributes to the longitudinal distribution of EPBs (Dao et al., 2011; Chang et
587 al., 2021; Chou et al., 2020b). It appears that the behavior of the diurnal tides in the neutral
588 winds significantly affects the day-to-day variability of EPBs. Future investigation of the
589 tidal forcing should advance our understanding of how atmospheric tides control the day-to-
590 day variability of EPBs.
591
592 **4. Conclusions**
593 We have investigated the day-to-day variability of EPBs using the coupled
594 SAMI3/WACCM-X model. Simulations reveal that EPBs developed on October 20 and 24
595 but not on October 22. We found that EPBs developed at midnight. Atmospheric gravity
596 waves and solar terminator waves are critical to midnight EPB development. They
597 significantly affect the neutral winds and electrodynamics, which could be responsible for the

day-to-day variability of midnight EPBs. The main findings of the present work are summarized as follows:

1. We found that gravity waves appear ubiquitous and could act as a natural seed for EPB development. The spacing between bottomside upwellings is consistent with the zonal scale of gravity wave perturbations in the zonal winds, suggesting that upwellings are related to gravity waves. However, upwelling growth requires sufficient ionospheric layer height, and the longitudinal variation of neutral wind becomes important.
2. Gravity waves do not necessarily lead to a quasiperiodic distribution of EPBs (e.g., Makela et al., 2010), depending on their zonal scale and wavefront alignment. The equatorward propagation of planar gravity waves causes irregular or isolated spatial distributions of EPBs, which partly explain why EPBs show isolated clusters separated by long distances on some nights but display a continuous distribution of EPB trains on other nights. The other reason is the longitudinal variation of ionospheric layer height due to meridional winds.
3. The longitudinal variation of meridional winds can affect the longitudinal variation of ionospheric layer height, which in turn controls the occurrence and longitudinal distribution of EPBs. We found that the converging winds associated with solar terminator waves along the magnetic equator can lead to a continuous distribution of EPBs spanning a large zonal distance. On the contrary, diverging winds due to MTM over the magnetic equator could lower the ionosphere, inhibit upwelling growth and result in irregular spatial distribution of EPBs.
4. As opposed to the post-sunset upward vertical drift enhancement due to the eastward wind, the westward winds associated with the dusk solar terminator waves or gravity waves play a vital role in the midnight upward drift enhancement and retrograde plasma flow. Both upward E×B drift and retrograde flow result in midnight vortex features, providing conditions favorable for upwelling growth and EPB development.
5. We found that solar terminator waves and/or gravity waves can be responsible not only for the seeding mechanism (e.g., Kelley et al., 1981), but also for collisional shear instability (Hysell and Kudeki, 2004). The dusk solar terminator waves (or gravity waves) generate a localized retrograde flow, merging with westward plasma flow in the bottomside ionosphere and leading to shear instability. The solar terminator waves and gravity waves also contribute to the large-scale EPB development (Figure 1a).
6. We found that the presence or absence of midnight EPBs connects to the westward winds driven by dusk solar terminator waves. Weak (or cessation of) westward winds prevented formation of midnight EPBs on October 20 because of weak upward E×B

drifts and retrograde flow, which in turn lead to lower ionospheric layer height and small growth rate.

This study provides a new perspective that the day-to-day variability of EPBs is significantly affected by the neutral wind perturbations driven by atmospheric waves. Therefore, ion drift, neutral wind, and atmospheric waves measurements in both hemispheres are helpful to the nowcasting of EPBs. Building a data assimilation system by incorporating state-of-the-art thermosphere data, such as ICON, into WACCM-X should improve the global neutral wind specification, advancing the capability of EPB nowcasting and forecasting (e.g., Hsu et al., 2021).

Acknowledgements

This research was supported by NASA grant 80NSSC20K0628. FS and SMcD acknowledge the support of NASA grant NNH21ZDA001N-LWS. This work was supported in part by high-performance computer time and resources from the DoD High Performance Computing Modernization Program.

Open Research

Data Availability Statement

The SAMI3/WACCM-X files are available at https://doi.org/10.5281/zenodo.7425959.

References

Aa, E., Zhang, S.-R., Erickson, P. J., Vierinen, J., Coster, A. J., Goncharenko, L. P., et al. (2022). Significant ionospheric hole and equatorial plasma bubbles after the 2022 Tonga volcano eruption. Space Weather, 20, e2022SW003101.

Abdu, M. A., E. Alam Kherani, I. S. Batista, E. R. de Paula, D. C. Fritts, and J. H. A. Sobral (2009), Gravity wave initiation of equatorial spread F/plasma bubble irregularities based on observational data from the SpreadFEx campaign, Ann. Geophys., 27, 2607, doi:10.5194/angeo-27-2607-2009.

Azeem, I., Yue, J., Hoffmann, L., Miller, S. D., Straka, W. C., and Crowley, G. (2015), Multisensor profiling of a concentric gravity wave event propagating from the troposphere to the ionosphere, Geophys. Res. Lett., 42, 7874– 7880, doi:10.1002/2015GL065903.

Bespalova, A. V., A. K. Fedorenko, O. K. Cheremnykh, and I. T. Zhuk (2016), Satellite observations of wave disturbances caused by moving solar terminator, J. Atmos. Sol. Terr. Phys., 140, 79– 85, doi:10.1016/j.jastp.2016.02.012.

Burke, W. J., Gentile, L. C., Huang, C. Y., Valladares, C. E., and Su, S. Y. (2004), Longitudinal variability of equatorial plasma bubbles observed by DMSP and ROCSAT-1, J. Geophys. Res., 109, A12301, doi:10.1029/2004JA010583.

Burke, W. J., de La Beaujardière, O., Gentile, L. C., Hunton, D. E., Pfaff, R. F., Roddy, P. A., Su, Y.-J., and Wilson, G. R. (2009), C/NOFS observations of plasma density and electric field irregularities at post-midnight local times, Geophys. Res. Lett., 36, L00C09, doi:10.1029/2009GL038879.

Chang, L. C., Salinas, C. C. J. H., Chiu, Y.-C., Jones, M., Rajesh, P. K., Chao, C.-K., et al. (2021). Implication of tidal forcing effects on the zonal variation of solstice equatorial plasma bubbles. Journal of Geophysical Research: Space Physics, 126, e2020JA028295. https://doi.org/10.1029/2020JA028295

Cherniak, I., and Zakharenkova, I. (2016), First observations of super plasma bubbles in Europe, Geophys. Res. Lett., 43, 11,137– 11,145, doi:10.1002/2016GL071421.

Chou, M. Y., Lin, C. C. H., Yue, J., Tsai, H. F., Sun, Y. Y., Liu, J. Y., and Chen, C. H. (2017), Concentric traveling ionosphere disturbances triggered by Super Typhoon Meranti (2016), Geophys. Res. Lett., 44, 1219– 1226, doi:10.1002/2016GL072205.

Chou, M.-Y., Pedatella, N. M., Wu, Q., Huba, J. D., Lin, C. C. H., Schreiner, W. S., et al. (2020a). Observation and simulation of the development of equatorial plasma bubbles: Post-sunset rise or upwelling growth?. Journal of Geophysical Research: Space Physics, 125, e2020JA028544. https://doi.org/10.1029/2020JA028544

Chou, M.-Y., Wu, Q., Pedatella, N. M., Cherniak, I., Schreiner, W. S., & Braun, J. (2020b).

690 Climatology of the equatorial plasma bubbles captured by FORMOSAT-3/COSMIC.
691 Journal of Geophysical Research: Space Physics, 125.
692 https://doi.org/10.1029/2019JA027680
693 Chou, M.-Y., Lin, C. C. H., & Huba, J. D. (2021). Modeling the disappearance of equatorial
694 plasma bubble by nighttime medium-scale traveling ionospheric disturbances.
695 Terrestrial, Atmospheric and Oceanic Sciences, 32(2), 217– 228.
696 https://doi.org/10.3319/TAO.2021.03.30.01
697 Coley WR, Stoneback RA, Heelis RA, Hairston MR (2014) Topside equatorial zonal ion
698 velocities measured by C/NOFS during rising solar activity. Ann Geophys 32:69–75.
699 https://doi.org/10.5194/angeo-32-69-2014
700 Dao, E., Kelley, M. C., Roddy, P., Retterer, J., Ballenthin, J. O., de La Beaujardiere, O., and
701 Su, Y.-J. (2011), Longitudinal and seasonal dependence of nighttime equatorial plasma
702 density irregularities during solar minimum detected on the C/NOFS satellite, Geophys.
703 Res. Lett., 38, L10104, doi:10.1029/2011GL047046.
704 Eastes, R. W., Solomon, S. C., Daniell, R. E., Anderson, D. N., Burns, A. G., England, S. L.,
705 et al. (2019). Global-scale observations of the equatorial ionization anomaly.
706 Geophysical Research Letters, 46. https://doi.org/10.1029/2019GL084199
707 Eccles, J. V. (2004), The effect of gravity and pressure in the electrodynamics of the low-
708 latitude ionosphere, J. Geophys. Res., 109, A05304, doi:10.1029/2003JA010023.
709 Ern, M., Preusse, P., Gille, J. C., Hepplewhite, C. L., Mlynczak, M. G., Russell, J. M., and
710 Riese, M. (2011), Implications for atmospheric dynamics derived from global
711 observations of gravity wave momentum flux in stratosphere and mesosphere, J.
712 Geophys. Res., 116, D19107, doi:10.1029/2011JD015821.
713 Fang, T.-W., Akmaev, R. A., Stoneback, R. A., Fuller-Rowell, T., Wang, H., and Wu, F.
714 (2016), Impact of midnight thermosphere dynamics on the equatorial ionospheric
715 vertical drifts, J. Geophys. Res. Space Physics, 121, 4858– 4868,
716 doi:10.1002/2015JA022282.
717 Fejer, B. G., D. T. Farley, C. A. Gonzales, R. F. Woodman, and C. Calderon (1981), F region
718 east–west drifts at Jicamarca, J. Geophys. Res., 86, 215.
719 Fejer, B. G., de Paula, E. R., Batista, I. S., Bonelli, E., & Woodman, R. F. (1989). Equatorial
720 F region vertical plasma drifts during solar maxima. Journal of Geophysical Research,
721 94(A9), 12,049–12,054. https://doi.org/10.1029/JA094iA09p12049
722 Gentile, L. C., Burke, W. J., & Rich, F. J. (2006). A climatology of equatorial plasma bubbles
723 from DMSP 1989–2004. Radio Science, 41, RS5S21.
724 https://doi.org/10.1029/2005RS003340
725 Gentile, L. C., Burke, W. J., Roddy, P. A., Retterer, J. M., and Tsunoda, R. T. (2011),
726 Climatology of plasma density depletions observed by DMSP in the dawn sector, J.
727 Geophys. Res., 116, A03321, doi:10.1029/2010JA016176.

Harding, B. J., Wu, Y.-J. J., Alken, P., Yamazaki, Y., Triplett, C. C., Immel, T. J., et al. (2022). Impacts of the January 2022 Tonga volcanic eruption on the ionospheric dynamo: ICON-MIGHTI and Swarm observations of extreme neutral winds and currents. Geophysical Research Letters, 49(9), e2022GL098577. https://doi.org/10.1029/2022GL098577

Heale, C. J., Inchin, P. A., & Snively, J. B. (2022). Primary versus secondary gravity wave responses at F-region heights generated by a convective source. Journal of Geophysical Research: Space Physics, 127, e2021JA029947. https://doi.org/10.1029/2021JA029947

Heelis, R. (2004). Electrodynamics in the low and middle latitude ionosphere: A tutorial. Journal of Atmospheric and Solar-Terrestrial Physics, 66(10), 825– 838. https://doi.org/10.1016/j.jastp.2004.01.034

Heelis, R. A., Stoneback, R., Earle, G. D., Haaser, R. A., and Abdu, M. A. (2010), Medium-scale equatorial plasma irregularities observed by Coupled Ion-Neutral Dynamics Investigation sensors aboard the Communication Navigation Outage Forecast System in a prolonged solar minimum, J. Geophys. Res., 115, A10321, doi:10.1029/2010JA015596.

Huba, J. D., Joyce, G., & Fedder, J. A. (2000). SAMI2 (Sami2 is another model of the ionosphere): A new low-latitude ionosphere model. Journal of Geophysical Research, 105(A10), 23,035–23,053.

Huba, J. D., and Joyce, G. (2010), Global modeling of equatorial plasma bubbles, Geophys. Res. Lett., 37, L17104, doi:10.1029/2010GL044281.

Huba, J. D., Drob, D. P., Wu, T.-W., and Makela, J. J. (2015), Modeling the ionospheric impact of tsunami-driven gravity waves with SAMI3: Conjugate effects, Geophys. Res. Lett., 42, 5719– 5726, doi:10.1002/2015GL064871.

Huba, J. D., Maute, A., & Crowley, G. (2017). SAMI3_ICON: Model of the ionosphere/plasmasphere system. Space Science Review, 212, 731. https://doi.org/10.1007/s11214-017-0415-z

Huba, J. D., & Liu, H.-L. (2020). Global modeling of equatorial spread F with SAMI3/WACCM-X. Geophysical Research Letters, 47, e2020GL088258.

Huba, J. D., Krall, J., & Drob, D. (2020). Modeling the impact of metallic ion layers on equatorial spread with SAMI3/ESF. Geophysical Research Letters, 47(5), e2020GL087224. https://doi.org/10.1029/2020GL087224

Huba, J. D., and Krall, J. (2013), Impact of meridional winds on equatorial spread F: Revisited, Geophys. Res. Lett., 40, 1268– 1272, doi:10.1002/grl.50292.

Huang, C.-S., La Beaujardière, O., Roddy, P. A., Hunton, D. E., Ballenthin, J. O., Hairston, M. R., and Pfaff, R. F. (2013), Large-scale quasiperiodic plasma bubbles: C/NOFS observations and causal mechanism, J. Geophys. Res. Space Physics, 118, 3602– 3612, doi:10.1002/jgra.50338.

766 Hsu, C.-T., N. Pedatella, and J. L. Anderson (2021), Impact of Thermospheric Wind Data
767 Assimilation on Ionospheric Electrodynamics using a Coupled Whole Atmosphere Data
768 Assimilation System. J. Geophys. Res. Space Physics. doi: 10.1029/2021JA029656
769 Hysell, D. L., and Kudeki, E. (2004), Collisional shear instability in the equatorial F region
770 ionosphere, J. Geophys. Res., 109, A11301, doi:10.1029/2004JA010636.
771 Hysell, D. L., E. Kudeki, and J. L. Chau (2005), Possible ionospheric preconditioning by
772 shear flow leading to equatorial spread F, Ann. Geophys., 23, 2647, doi:10.5194/angeo-
773 23-2647-2005.
774 Hysell, D. L., Hedden, R. B., Chau, J. L., Galindo, F. R., Roddy, P. A., and Pfaff, R. F.
775 (2009),
776 Comparing F region ionospheric irregularity observations from C/NOFS and Jicamarca,
777 Geophys. Res. Lett., 36, L00C01, doi:10.1029/2009GL038983.
778 Hysell, D. L., Fang, T. W., & Fuller-Rowell, T. J. (2022). Modeling equatorial F-region
779 ionospheric instability using a regional ionospheric irregularity model and WAM-IPE.
780 Journal of Geophysical Research: Space Physics, 127, e2022JA030513.
781 https://doi.org/10.1029/2022JA030513
782 Kil, H., Heelis, R. A., Paxton, L. J., and Oh, S.-J. (2009), Formation of a plasma depletion
783 shell in the equatorial ionosphere, J. Geophys. Res., 114, A11302,
784 doi:10.1029/2009JA014369.
785 Kelley, M. C., Larsen, M. F., LaHoz, C., and McClure, J. P. (1981), Gravity wave initiation
786 of equatorial spread F: A case study, J. Geophys. Res., 86(A11), 9087– 9100,
787 doi:10.1029/JA086iA11p09087.
788 Kelley, M. C., Makela, J. J., Paxton, L. J., Kamalabadi, F., Comberiate, J. M., and Kil, H.
789 (2003), The first coordinated ground- and space-based optical observations of equatorial
790 plasma bubbles, Geophys. Res. Lett., 30, 1766, doi:10.1029/2003GL017301, 14.
791 Kelly, M. A., Comberiate, J. M., Miller, E. S., and Paxton, L. J. (2014), Progress toward
792 forecasting of space weather effects on UHF SATCOM after Operation Anaconda,
793 Space Weather, 12, 601– 611, doi:10.1002/2014SW001081.
794 Kintner, P. M., Ledvina, B. M., and de Paula, E. R. (2007), GPS and ionospheric
795 scintillations, Space Weather, 5, S09003, doi:10.1029/2006SW000260.
796 Krall, J., Huba ,J.D., Joyce, G., & Zalesak, S.T.(2009).Three- dimensional simulation of
797 equatorial spread F with meridional wind effects. Annales Geophysicae, 27, 1821
798 Krall, J., Huba, J. D., Joyce, G., and Hei, M. (2013), Simulation of the seeding of equatorial
799 spread F by circular gravity waves, Geophys. Res. Lett., 1– 5,
800 doi:10.1029/2012GL054022.
801 Kudeki, E., and Bhattacharyya, S. (1999), Postsunset vortex in equatorial F-region plasma
802 drifts and implications for bottomside spread-F, J. Geophys. Res., 104(A12), 28163–
803 28170, doi:10.1029/1998JA900111.

804 Kudeki, E., A. Akgiray, M. Milla, J. L. Chau, and D. L. Hysell (2007), Equatorial spread F
805 initiation: Post-sunset vortex thermospheric winds, gravity waves, J. Atmos. Sol. Terr.
806 Phys., 69, 2416–2427.
807 Lin, C. H., Liu, J. Y., Fang, T. W., Chang, P. Y., Tsai, H. F., Chen, C. H., and Hsiao, C. C.
808 (2007), Motions of the equatorial ionization anomaly crests imaged by FORMOSAT-
809 3/COSMIC, Geophys. Res. Lett., 34, L19101, doi:10.1029/2007GL030741.
810 Liu, H., Lühr, H., and Watanabe, S. (2009), A solar terminator wave in thermospheric wind
811 and density simultaneously observed by CHAMP, Geophys. Res. Lett., 36, L10109,
812 doi:10.1029/2009GL038165.
813 Liu, H.-L., Bardeen, C. G., Foster, B. T., Lauritzen, P., Liu, J., Lu, G., … Wang, W. (2018).
814 Development and validation of the Whole Atmosphere Community Climate Model with
815 thermosphere and ionosphere extension (WACCM-X 2.0). Journal of Advances in
816 Modeling Earth Systems, 10, 381– 402. https://doi.org/10.1002/2017MS001232
817 Makela, J. J., Vadas, S. L., Muryanto, R., Duly, T., & Crowley, G. (2010). Periodic spacing
818 between consecutive equatorial plasma bubbles. Geophysical Research Letters, 37,
819 L14103. https://doi.org/10.1029/2010GL043968
820 Maute, A., Richmond, A. D., and Roble, R. G. (2012), Sources of low-latitude ionospheric E
821 × B drifts and their variability, J. Geophys. Res., 117, A06312,
822 doi:10.1029/2011JA017502.
823 McDonald, S. E., F. Sassi, and A. J. Mannucci (2015), SAMI3/SD-WACCM-X simulations
824 of ionospheric variability during northern winter 2009, Space Weather, 13, 568–584,
825 doi:10.1002/2015SW001223.
826 McDonald, S. E., Sassi, F., Tate, J., McCormack, J., Kuhl, D. D., Drob, D. P., Metzler, C., &
827 Mannucci, A. J. (2018). Impact of non-migrating tides on the low latitude ionosphere
828 during a sudden stratospheric warming event in January 2010. Journal of Atmospheric
829 and Solar-Terrestrial Physics, 171, 188– 200.
830 https://doi.org/10.1016/j.jastp.2017.09.012
831 Miller, E. S., Makela, J. J., and Kelley, M. C. (2009), Seeding of equatorial plasma depletions
832 by polarization electric fields from middle latitudes: Experimental evidence, Geophys.
833 Res. Lett., 36, L18105, doi:10.1029/2009GL039695.
834 Nishioka, M., Saito, A., and Tsugawa, T. (2008), Occurrence characteristics of plasma
835 bubble derived from global ground-based GPS receiver networks, J. Geophys. Res., 113,
836 A05301, doi:10.1029/2007JA012605.
837 Nishioka, M., Otsuka, Y., Shiokawa, K., Tsugawa, T., Effendy, , Supnithi, P., Nagatsuma, T.,
838 and Murata, K. T. (2012), On post-midnight field-aligned irregularities observed with a
839 30.8-MHz radar at a low latitude: Comparison withF-layer altitude near the
840 geomagnetic equator, J. Geophys. Res., 117, A08337, doi:10.1029/2012JA017692.
841 Otsuka, Y., Shiokawa, K., Ogawa, T., & Wilkinson, P. (2002). Geomagnetic conjugate

observations of equatorial airglow depletions. Geophysical Research Letters, 29(15), 43-1– 43-4. https://doi.org/10.1029/2002GL015347

Otsuka, Y. (2018). Review of the generation mechanisms of post-midnight irregularities in the equatorial and low-latitude ionosphere. Progress in Earth and Planetary Science, 5, 57. https://doi.org/10.1186/s40645-018-0212-7

Perkins, F. (1973), Spread F and ionospheric currents, J. Geophys. Res., 78(1), 218– 226, doi:10.1029/JA078i001p00218.

Rajesh, P. K., Lin, C. H., Chen, C. H., Lin, J. T., Matsuo, T., Chou, M. Y., Chen, W. H., Chang, M. T., and You, C. F. (2017), Equatorial plasma bubble generation/inhibition during 2015 St. Patrick's Day storm, Space Weather, 15, 1141– 1150, doi:10.1002/2017SW001641.

Rajesh, P. K., Lin, C. C. H., Lin, J. T., Lin, C. Y., Liu, J. Y., Matsuo, T., et al. (2022). Extreme poleward expanding super plasma bubbles over Asia-Pacific region triggered by Tonga volcano eruption during the recovery-phase of geomagnetic storm. Geophysical Research Letters, 49, e2022GL099798. https://doi.org/10.1029/2022GL099798

Retterer, J. M., Decker, D. T., Borer, W. S., Daniell, R. E., and Fejer, B. G. (2005), Assimilative modeling of the equatorial ionosphere for scintillation forecasting: Modeling with vertical drifts, J. Geophys. Res., 110, A11307, doi:10.1029/2002JA009613.

Retterer, J. M., and P. Roddy (2014), Faith in a seed: On the origin of equatorial plasma bubbles, Ann. Geophys., 32, 485–498, doi:10.5194/angeo-32-485-2014.

Rishbeth, H. (1971), The F-layer dynamo, Planet. Space Sci., 19, 263–267, doi:10.1016/0032-0633(71)90205-4.

Richmond, A. D., T.-W. Fang, and A. Maute (2015), Electrodynamics of the equatorial evening ionosphere: 1. Importance of winds in different regions, J. Geophys. Res. Space Physics, 120, 2118–2132, doi:10.1002/2014JA020934.

Singh, S., Johnson, F. S., and Power, R. A. (1997), Gravity wave seeding of equatorial plasma bubbles, J. Geophys. Res., 102(A4), 7399– 7410, doi:10.1029/96JA03998.

Saito, S., and Maruyama, T. (2007), Large-scale longitudinal variation in ionospheric height and equatorial spread F occurrences observed by ionosondes, Geophys. Res. Lett., 34, L16109, doi:10.1029/2007GL030618.

Scherliess, L., and Fejer, B. G. (1999), Radar and satellite global equatorial F region vertical drift model, J. Geophys. Res., 104(A4), 6829– 6842, doi:10.1029/1999JA900025.

Stoneback, R. A., Heelis, R. A., Burrell, A. G., Coley, W. R., Fejer, B. G., and Pacheco, E. (2011), Observations of quiet time vertical ion drift in the equatorial ionosphere during the solar minimum period of 2009, *J. Geophys. Res.*, 116, A12327, doi:10.1029/2011JA016712.

880 Su, Y.-J., Retterer, J. M., de La Beaujardière, O., Burke, W. J., Roddy, P. A., Pfaff, R. F.,
881 Wilson, G. R., and Hunton, D. E. (2009), Assimilative modeling of equatorial plasma
882 depletions observed by C/NOFS, Geophys. Res. Lett., 36, L00C02,
883 doi:10.1029/2009GL038946.
884 Sultan, P. J. (1996), Linear theory and modeling of the Rayleigh-Taylor instability leading to
885 the occurrence of the equatorial spread F, J. Geophys. Res., 101, 26,875–26,891,
886 doi:10.1029/96JA00682.
887 Tsunoda, R. T., Livingston, R. C., and Rino, C. L. (1981), Evidence of a velocity shear in
888 bulk plasma motion associated with the post-sunset rise of the equatorial F-layer,
889 Geophys. Res. Lett., 8(7), 807– 810, doi:10.1029/GL008i007p00807.
890 Tsunoda, R. T. (2007), Seeding of equatorial plasma bubbles with electric fields from an Es-
891 layer instability, J. Geophys. Res., 112, A06304, doi:10.1029/2006JA012103.
892 Tsunoda, R. T. (2010), On seeding equatorial spread F: Circular gravity waves, Geophys. Res.
893 Lett., 37, L10104, doi:10.1029/2010GL043422.
894 Tsunoda, R. T. (2015). Upwelling: A unit of disturbance in equatorial spread F. Progress in
895 Earth and Planetary Science, 2, 9. https://doi-org.cuucar.idm.oclc.org/10.1186/s40645-
896 015-0038-5
897 Tsunoda, R. T., Nguyen, T. T., and Le, M. H. (2015), Effects of tidal forcing, conductivity
898 gradient, and active seeding on the climatology of equatorial spread F over Kwajalein, J.
899 Geophys. Res. Space Physics, 120, 632– 653, doi:10.1002/2014JA020762.
900 Tsunoda, R. T., Saito, S., & Nguyen, T. T. (2018). Post-sunset rise of equatorial F layer—or
901 upwelling growth? Progress in Earth and Planetary Science, 5, 22. https://doi-
902 org.cuucar.idm.oclc.org/10.1186/s40645-018-0179-4
903 Tsunoda, R.T. (2021). Observations of Equatorial Spread F . In Ionosphere Dynamics and
904 Applications (eds C. Huang, G. Lu, Y. Zhang and L.J. Paxton).
905 https://doi.org/10.1002/9781119815617.ch11
906 Tulasi Ram, S., Yamamoto, M., Tsunoda, R. T., Chau, H. D., Hoang, T. L., Damtie, B.,
907 Wassaie, M., Yatini, C. Y., Manik, T., and Tsugawa, T. (2014), Characteristics of large-
908 scale wave structure observed from African and Southeast Asian longitudinal sectors, J.
909 Geophys. Res. Space Physics, 119, 2288– 2297, doi:10.1002/2013JA019712.
910 Vadas, S. L., & Fritts, D. C. (2004). Thermospheric responses to gravity waves arising from
911 mesoscale convective complexes. Journal of Atmospheric and Solar - Terrestrial Physics,
912 66, 781–804. https://doi.org/10.1016/j.jastp.2004.01.025
913 Vadas, S. L., and H. Liu (2009), Generation of large-scale gravity waves and neutral winds in
914 the thermosphere from the dissipation of convectively generated gravity waves, J.
915 Geophys. Res., 114, A10310, doi:10.1029/2009JA014108.
916 Vadas, S. L. & Azeem, I. (2021). Concentric secondary gravity waves in the thermosphere

and ionosphere over the continental United States on March 25–26, 2015 from deep Convection. Journal of Geophysical Research: Space Physics, 126, e2020JA028275. https://doi.org/10.1029/2020JA028275

Varney, R. H., Kelley, M. C., and Kudeki, E. (2009), Observations of electric fields associated with internal gravity waves, J. Geophys. Res., 114, A02304, doi:10.1029/2008JA013733.

Woodman, R. F., and La Hoz, C. (1976), Radar observations of F region equatorial irregularities, J. Geophys. Res., 81(31), 5447– 5466, doi:10.1029/JA081i031p05447.

Xiong, C., Stolle, C., and Lühr, H. (2016), The Swarm satellite loss of GPS signal and its relation to ionospheric plasma irregularities, Space Weather, 14, 563– 577, doi:10.1002/2016SW001439.

Yeh, KC, Liu C-H (1982) Radio wave scintillations in the ionosphere. Proc IEEE 70:324–360.

Yizengaw, E., Moldwin, M. B., Sahai, Y., and de Jesus, R. (2009), Strong postmidnight equatorial ionospheric anomaly observations during magnetically quiet periods, J. Geophys. Res., 114, A12308, doi:10.1029/2009JA014603.

Yizengaw, E., Retterer, J., Pacheco, E. E., Roddy, P., Groves, K., Caton, R., and Baki, P. (2013), Postmidnight bubbles and scintillations in the quiet-time June solstice, Geophys. Res. Lett., 40, 5592– 5597, doi:10.1002/2013GL058307.

Yokoyama, T., Pfaff, R. F., Roddy, P. A., Yamamoto, M., and Otsuka, Y. (2011), On postmidnight low-latitude ionospheric irregularities during solar minimum: 2. C/NOFS observations and comparisons with the Equatorial Atmosphere Radar, J. Geophys. Res., 116, A11326, doi:10.1029/2011JA016798.

Yokoyama, T., Jin, H., and Shinagawa, H. (2015), West wall structuring of equatorial plasma bubbles simulated by three-dimensional HIRB model, J. Geophys. Res. Space Physics, 120, 8810– 8816, doi:10.1002/2015JA021799.

Yokoyama, T. (2017). A review of the numerical simulation of equatorial plasma bubbles toward scintillation evaluation and forecasting. Progress in Earth and Planetary Science, 4, 37. https://doi.org/10.1186/s40645-017-0153-6

Yue, J., Miller, S. D., Straka, W. C., Noh, Y.-J., Chou, M.-Y., Kahn, R., & Flower, V. (2022). La Soufriere volcanic eruptions launched gravity waves into space. Geophysical Research Letters, 49, e2022GL097952. https://doi.org/10.1029/2022GL097952

Zabotin, N. A., Godin, O. A., and Bullett, T. W. (2016), Oceans are a major source of waves in the thermosphere, J. Geophys. Res. Space Physics, 121, 3452– 3463, doi:10.1002/2016JA022357.

Zhang, S.-R., Erickson, P. J., Gasque, L. C., Aa, E., Rideout, W., Vierinen, J., et al. (2021). Electrified postsunrise ionospheric perturbations at Millstone Hill. Geophysical Research Letters, 48, e2021GL095151. https://doi.org/10.1029/2021GL095151

Figure Captions:

Figure 1. TEC maps from the SAMI3/WACCM-X simulation at 08:00, 08:00, and 10:00 UT on October 20, 22, and 24, respectively, in 2020. Clear dark band structures related to EPBs can be identified on October 20 and 24 with irregular and regular spatial distribution, respectively. EPBs are confined within 63.6°-136.5°W. The white line indicates the magnetic equator. The dashed lines indicate the longitudes from 30° -180°W with 30° interval.

Figure 2. The electron density (top panels, log scale) and zonal wind perturbations extracted by high-pass filter (bottom panels) as a function of longitude and altitude along the magnetic equator at 07:05, 07:00, and 07:00 UT on October 20, 22, and 24 in 2020. The black arrows denote the locations of upwellings and EPBs.

Figure 3. The neutral temperature perturbations from the WACCM-X simulation on October 20 (left panel), 22 (middle panel), and 24 (right panel). The green line indicates the magnetic equator.

Figure 4. The electron density (top panels, log scale), vertical E×B drift (middle panels) and zonal E×B drift (bottom panels) from the SAMI3/WACCM-X simulation as a function of longitude (local time) and altitude along the magnetic equator at 05:00, 05:30, 06:00, 07:00 and 08:00 UT on October 20, 2020.

Figure 5. Meridional (top panels) and zonal (bottom panels) winds from the WACCM-X simulation as a function of longitude (local time) and latitude at ~460 km at 05:00, 05:30, 06:00, 07:00 and 08:00 UT on October 20, 2020. The white lines denote the magnetic latitudes at 0° and ±25°.

Figure 6. The electron density (top panels, log scale), vertical E×B drift (middle panels) and zonal E×B drift (bottom panels) from the SAMI3/WACCM-X simulations as a function of longitude (local time) and altitude along the magnetic equator at 05:00, 06:00, 07:00, 08:00 and 09:00 UT on October 22, 2020.

Figure 7. Meridional (top panels) and zonal (bottom panels) winds from the WACCM-X simulations as a function of longitude (local time) and latitude at ~460 km at 05:00, 06:00, 07:00, 08:00 and 09:00 UT on October 22, 2020. The white lines denote the magnetic latitudes at 0° and ±25°.

Figure 8. Same as Figure 6, but for October 24, 2020.

Figure 9. Same as Figure 7, but for October 24, 2020.

Figure 10. Zonal (top panels) and vertical/meridional E×B drifts (bottom panels) as a function of latitude and altitude along the magnetic longitudes of 337.65°, 346.05°, and 357.45° (~ 95.3°W, 86.86°W, and 75.25°W at the magnetic equator) at 05:00 UT on October 20, 22, and 24, respectively.

Figure 11. Schematic of upward and westward (retrograde flow) E×B drifts generated by westward wind associated with solar terminator wave/gravity waves in the northern hemisphere.

Figure 12. A schematic representation of the coupled processes controlling the midnight EPB development.

Figure 13. Meridional winds at ~460 km altitude from the WACCM-X simulation at 05:00 UT on October 20 (top panel), 22 (middle panel), and 24 (bottom panel), 2020. The white line indicates the magnetic equator. The shaded area represents dawn-dusk solar terminators. The dashed lines indicate the wavefronts of solar terminator waves.

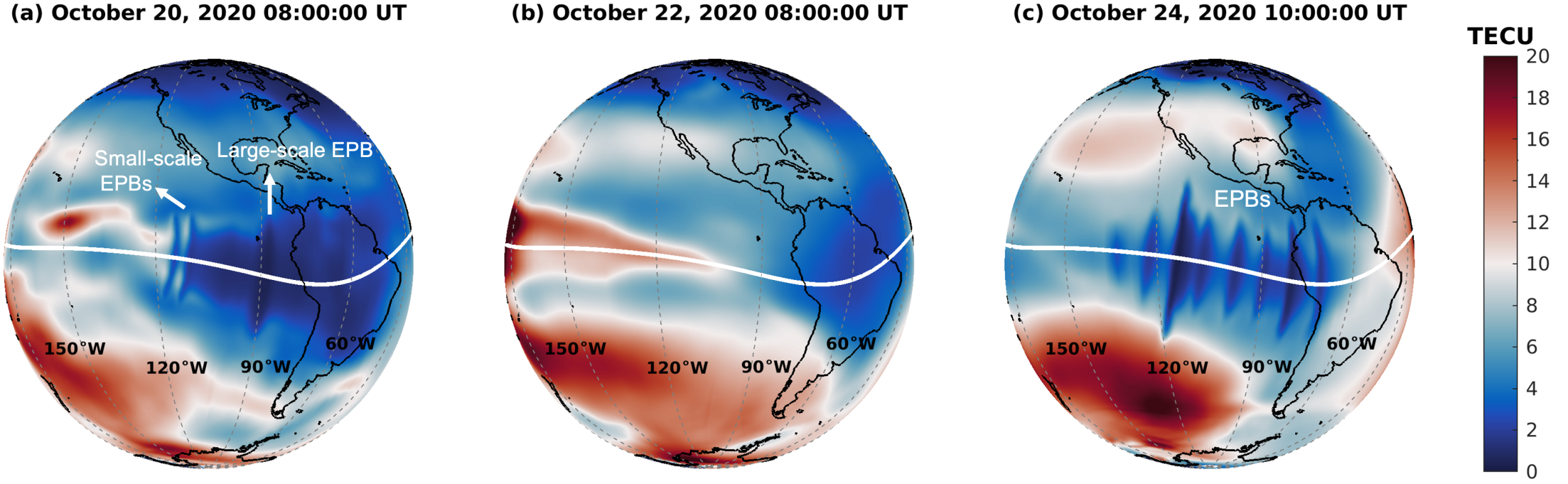
(a) October 20, 2020 08:00:00 UT
(b) October 22, 2020 08:00:00 UT
(c) October 24, 2020 10:00:00 UT
TECU
20
18
16
14
12
10
8
6
4
2
0
Small-scale EPBs
Large-scale EPB
EPBs
150°W
120°W
90°W
60°W

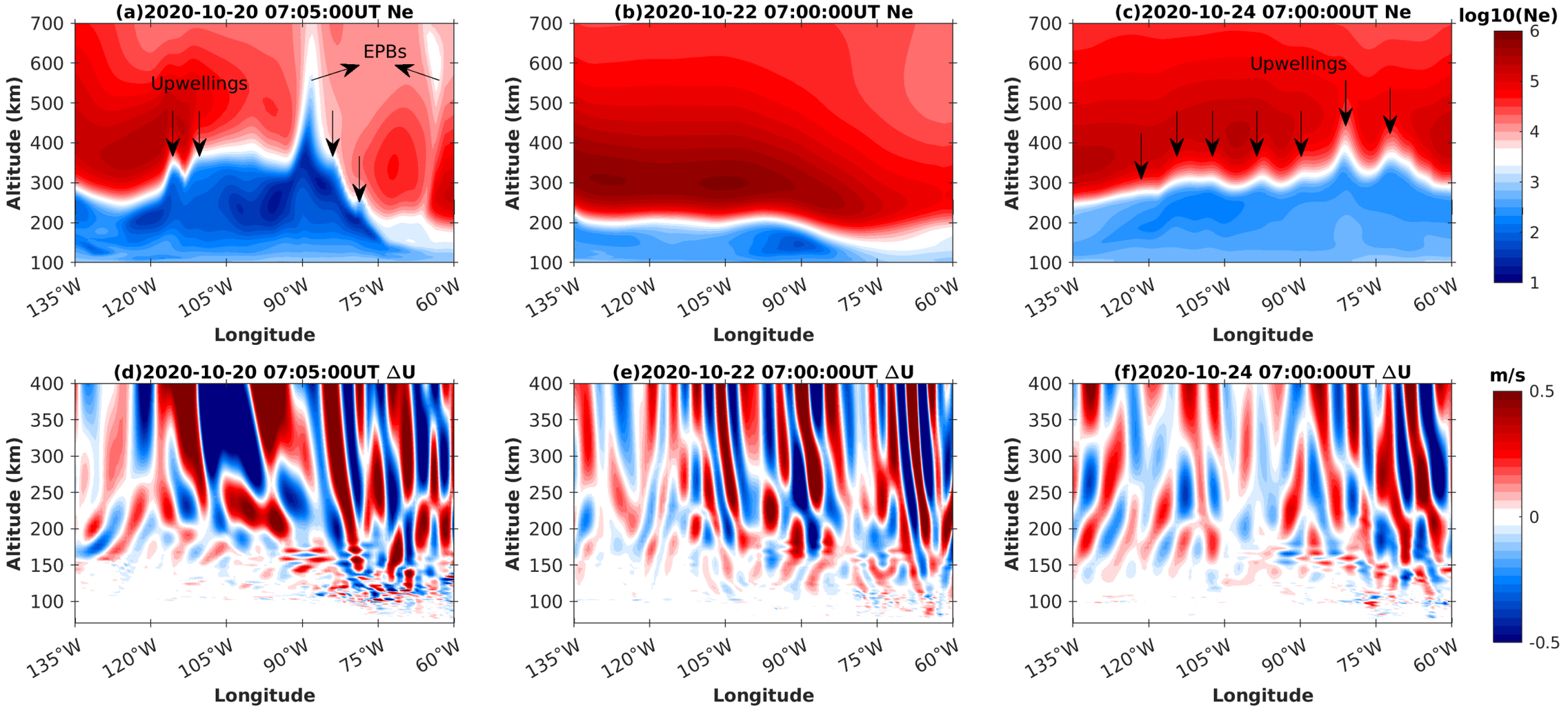
(a)2020-10-20 07:05:00UT Ne
(b)2020-10-22 07:00:00UT Ne
(c)2020-10-24 07:00:00UT Ne
log10(Ne)
Upwellings
EPBs
Altitude (km)
Longitude
(d)2020-10-20 07:05:00UT ΔU
(e)2020-10-22 07:00:00UT ΔU
(f)2020-10-24 07:00:00UT ΔU
m/s
135°W
120°W
105°W
90°W
75°W
60°W

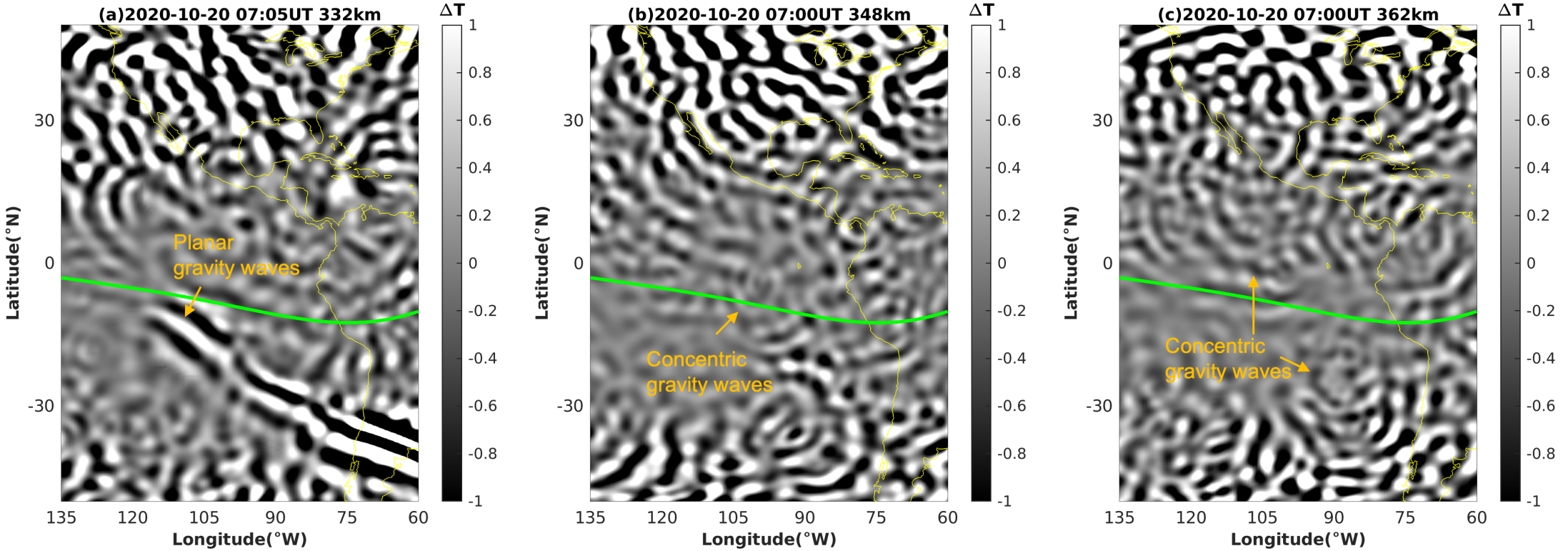
(a)2020-10-20 07:05UT 332km
(b)2020-10-20 07:00UT 348km
(c)2020-10-20 07:00UT 362km
ΔT
1
0.8
0.6
0.4
0.2
0
-0.2
-0.4
-0.6
-0.8
-1
Latitude(°N)
30
0
-30
135
120
105
90
75
60
Longitude(°W)
Planar
gravity waves
Concentric
gravity waves
Concentric
gravity waves

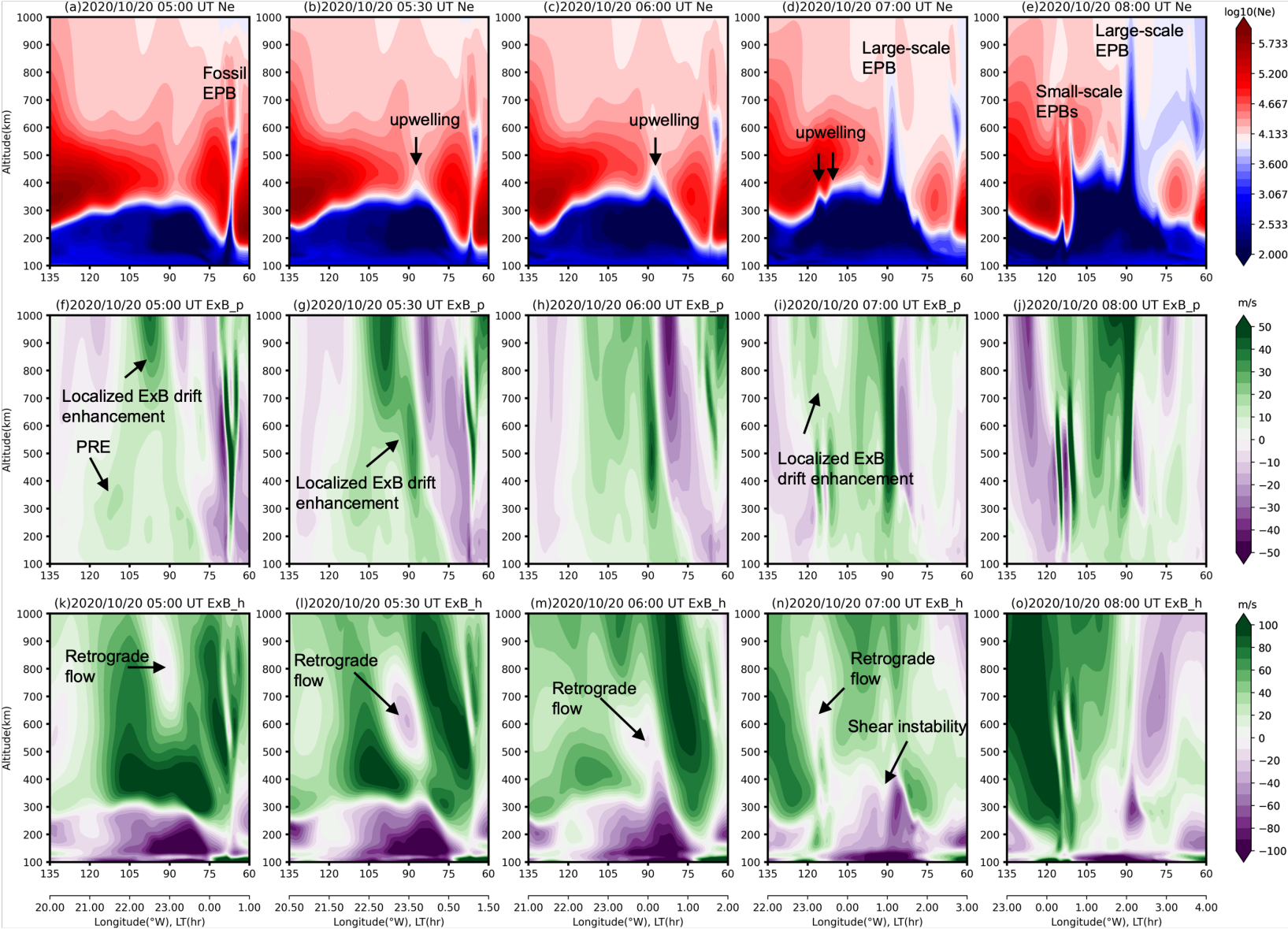
(a)2020/10/20 05:00 UT Ne
(b)2020/10/20 05:30 UT Ne
(c)2020/10/20 06:00 UT Ne
(d)2020/10/20 07:00 UT Ne
(e)2020/10/20 08:00 UT Ne
log10(Ne)
Fossil EPB
upwelling
upwelling
Large-scale EPB
upwelling
Large-scale EPB
Small-scale EPBs
(f)2020/10/20 05:00 UT ExB_p
(g)2020/10/20 05:30 UT ExB_p
(h)2020/10/20 06:00 UT ExB_p
(i)2020/10/20 07:00 UT ExB_p
(j)2020/10/20 08:00 UT ExB_p
m/s
Localized ExB drift enhancement
PRE
Localized ExB drift enhancement
Localized ExB drift enhancement
(k)2020/10/20 05:00 UT ExB_h
(l)2020/10/20 05:30 UT ExB_h
(m)2020/10/20 06:00 UT ExB_h
(n)2020/10/20 07:00 UT ExB_h
(o)2020/10/20 08:00 UT ExB_h
m/s
Retrograde flow
Retrograde flow
Retrograde flow
Retrograde flow
Shear instability
Altitude(km)
Longitude(°W), LT(hr)

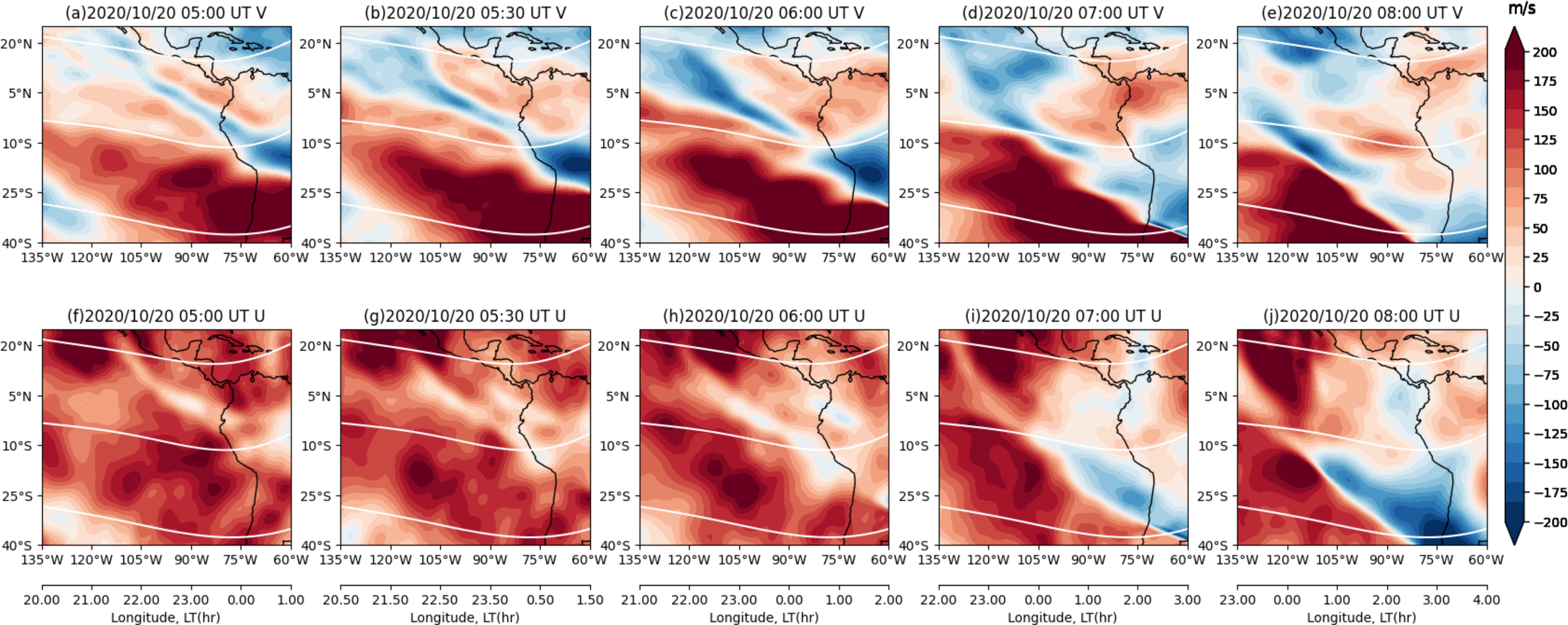
(a)2020/10/20 05:00 UT V
(b)2020/10/20 05:30 UT V
(c)2020/10/20 06:00 UT V
(d)2020/10/20 07:00 UT V
(e)2020/10/20 08:00 UT V
(f)2020/10/20 05:00 UT U
(g)2020/10/20 05:30 UT U
(h)2020/10/20 06:00 UT U
(i)2020/10/20 07:00 UT U
(j)2020/10/20 08:00 UT U
20°N
5°N
10°S
25°S
40°S
135°W 120°W 105°W 90°W 75°W 60°W
m/s
200
175
150
125
100
75
50
25
0
−25
−50
−75
−100
−125
−150
−175
−200
20.00 21.00 22.00 23.00 0.00 1.00
20.50 21.50 22.50 23.50 0.50 1.50
21.00 22.00 23.00 0.00 1.00 2.00
22.00 23.00 0.00 1.00 2.00 3.00
23.00 0.00 1.00 2.00 3.00 4.00
Longitude, LT(hr)

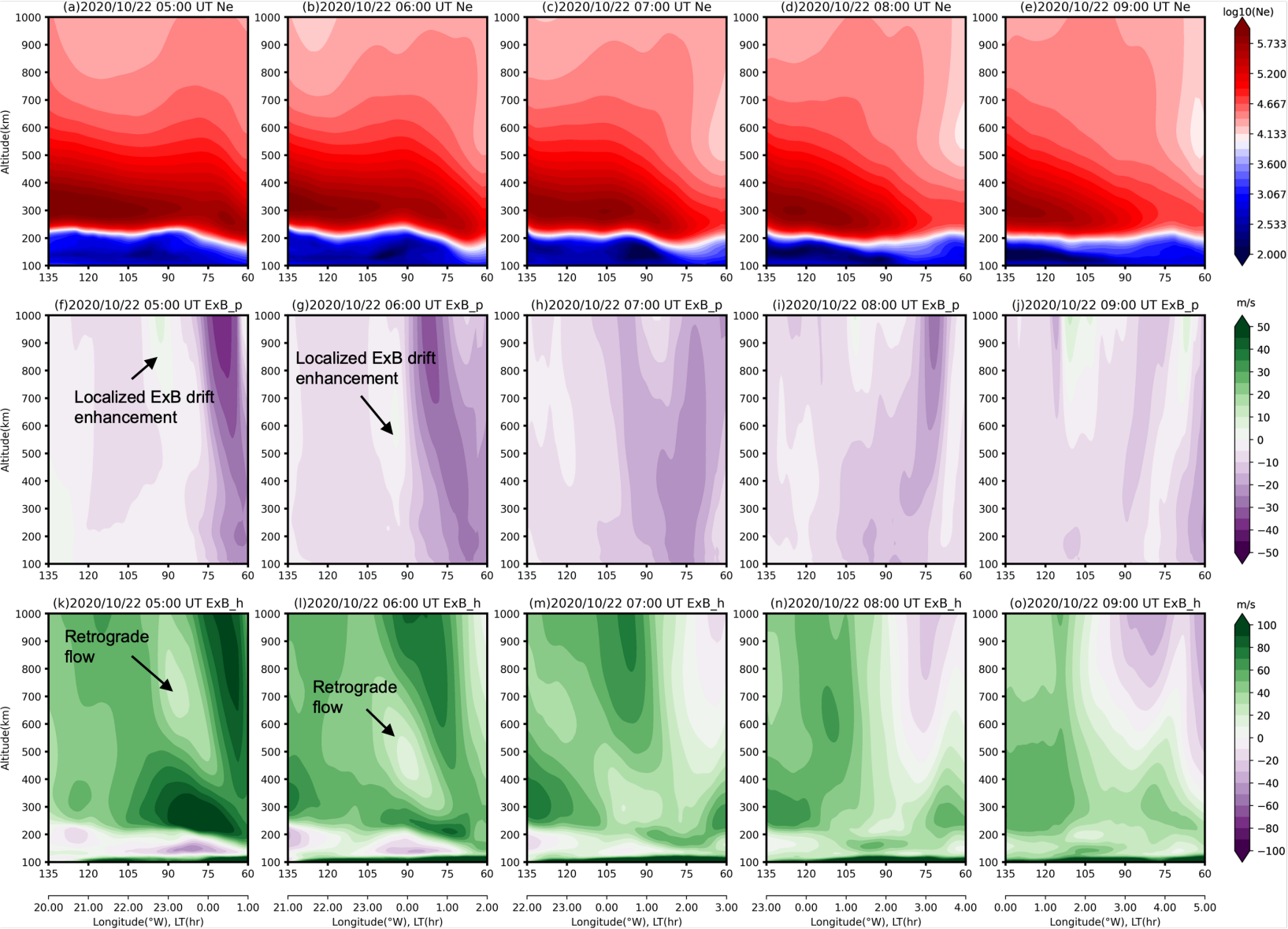
(a)2020/10/22 05:00 UT Ne
(b)2020/10/22 06:00 UT Ne
(c)2020/10/22 07:00 UT Ne
(d)2020/10/22 08:00 UT Ne
(e)2020/10/22 09:00 UT Ne
log10(Ne)
5.733
5.200
4.667
4.133
3.600
3.067
2.533
2.000
(f)2020/10/22 05:00 UT ExB_p
(g)2020/10/22 06:00 UT ExB_p
(h)2020/10/22 07:00 UT ExB_p
(i)2020/10/22 08:00 UT ExB_p
(j)2020/10/22 09:00 UT ExB_p
Localized ExB drift enhancement
Localized ExB drift enhancement
m/s
50
40
30
20
10
0
−10
−20
−30
−40
−50
(k)2020/10/22 05:00 UT ExB_h
(l)2020/10/22 06:00 UT ExB_h
(m)2020/10/22 07:00 UT ExB_h
(n)2020/10/22 08:00 UT ExB_h
(o)2020/10/22 09:00 UT ExB_h
Retrograde flow
Retrograde flow
m/s
100
80
60
40
20
0
−20
−40
−60
−80
−100
Altitude(km)
100
200
300
400
500
600
700
800
900
1000
135 120 105 90 75 60
20.00 21.00 22.00 23.00 0.00 1.00
21.00 22.00 23.00 0.00 1.00 2.00
22.00 23.00 0.00 1.00 2.00 3.00
23.00 0.00 1.00 2.00 3.00 4.00
0.00 1.00 2.00 3.00 4.00 5.00
Longitude(°W), LT(hr)

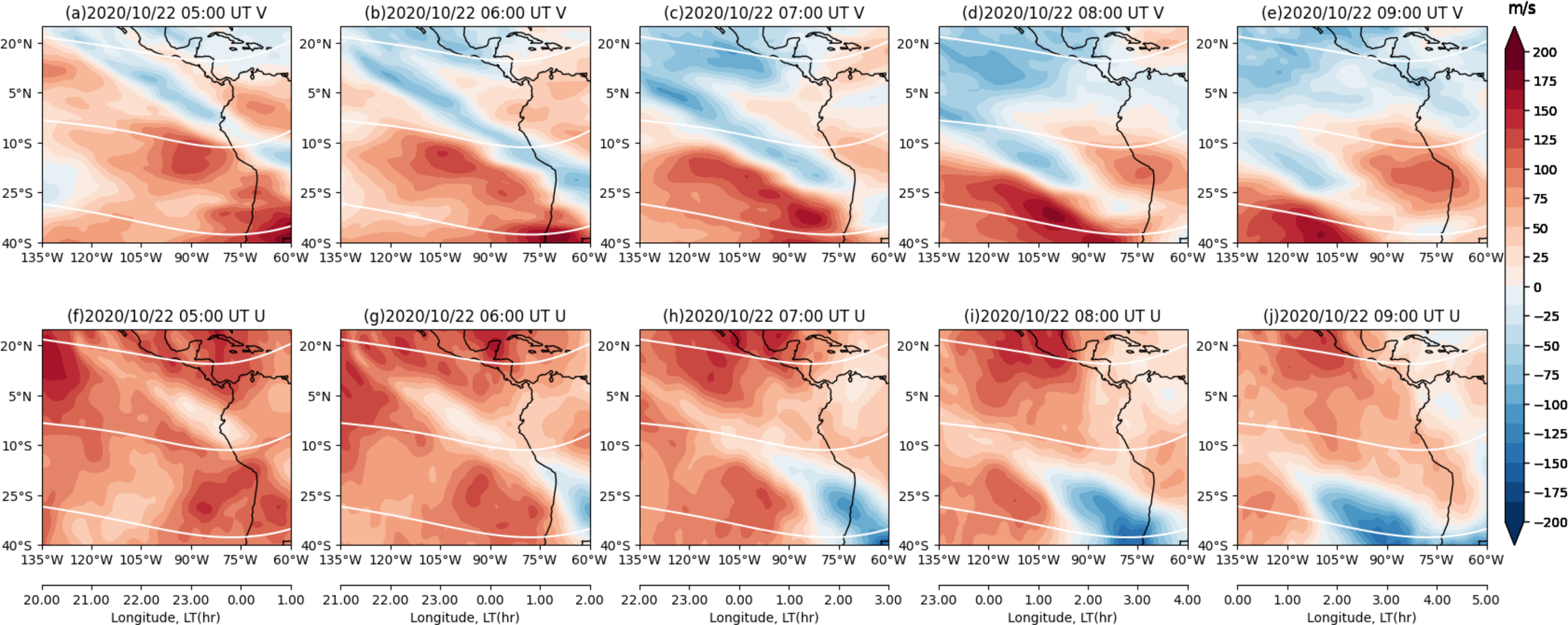
(a)2020/10/22 05:00 UT V
(b)2020/10/22 06:00 UT V
(c)2020/10/22 07:00 UT V
(d)2020/10/22 08:00 UT V
(e)2020/10/22 09:00 UT V
(f)2020/10/22 05:00 UT U
(g)2020/10/22 06:00 UT U
(h)2020/10/22 07:00 UT U
(i)2020/10/22 08:00 UT U
(j)2020/10/22 09:00 UT U
m/s
200
175
150
125
100
75
50
25
0
−25
−50
−75
−100
−125
−150
−175
−200
20°N
5°N
10°S
25°S
40°S
135°W 120°W 105°W 90°W 75°W 60°W
20.00 21.00 22.00 23.00 0.00 1.00
21.00 22.00 23.00 0.00 1.00 2.00
22.00 23.00 0.00 1.00 2.00 3.00
23.00 0.00 1.00 2.00 3.00 4.00
0.00 1.00 2.00 3.00 4.00 5.00
Longitude, LT(hr)

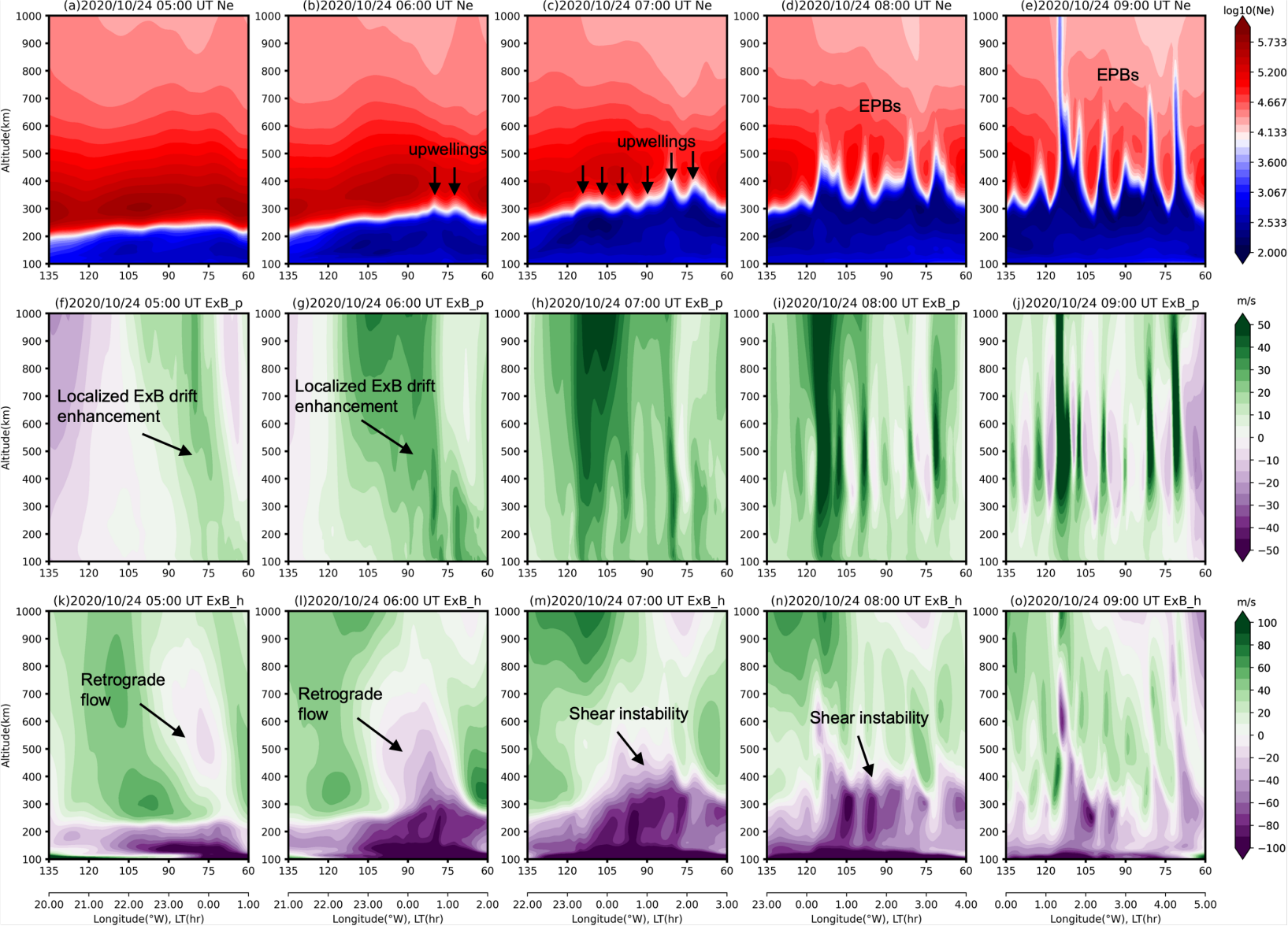
(a)2020/10/24 05:00 UT Ne
(b)2020/10/24 06:00 UT Ne
(c)2020/10/24 07:00 UT Ne
(d)2020/10/24 08:00 UT Ne
(e)2020/10/24 09:00 UT Ne
log10(Ne)
upwellings
upwellings
EPBs
EPBs
(f)2020/10/24 05:00 UT ExB_p
(g)2020/10/24 06:00 UT ExB_p
(h)2020/10/24 07:00 UT ExB_p
(i)2020/10/24 08:00 UT ExB_p
(j)2020/10/24 09:00 UT ExB_p
m/s
Localized ExB drift enhancement
Localized ExB drift enhancement
(k)2020/10/24 05:00 UT ExB_h
(l)2020/10/24 06:00 UT ExB_h
(m)2020/10/24 07:00 UT ExB_h
(n)2020/10/24 08:00 UT ExB_h
(o)2020/10/24 09:00 UT ExB_h
m/s
Retrograde flow
Retrograde flow
Shear instability
Shear instability
Altitude(km)
Longitude(°W), LT(hr)

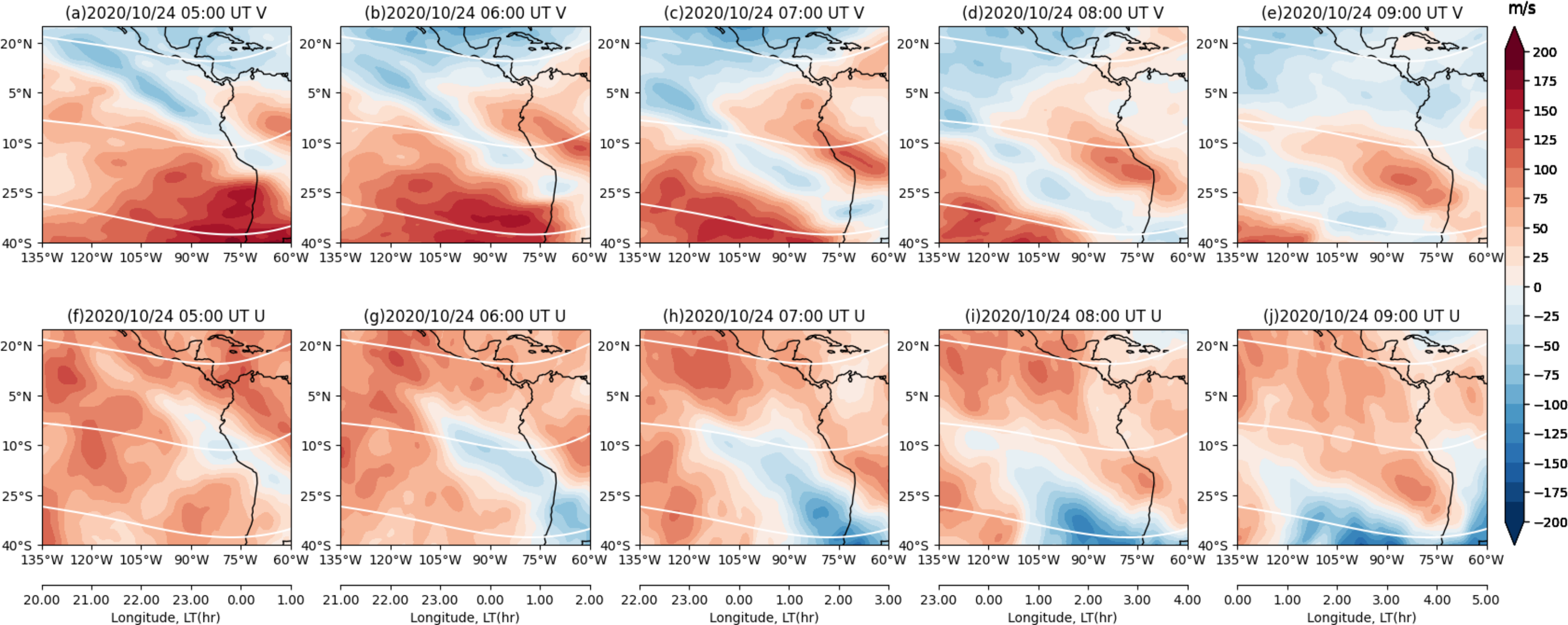
(a)2020/10/24 05:00 UT V
(b)2020/10/24 06:00 UT V
(c)2020/10/24 07:00 UT V
(d)2020/10/24 08:00 UT V
(e)2020/10/24 09:00 UT V
(f)2020/10/24 05:00 UT U
(g)2020/10/24 06:00 UT U
(h)2020/10/24 07:00 UT U
(i)2020/10/24 08:00 UT U
(j)2020/10/24 09:00 UT U
m/s
200
175
150
125
100
75
50
25
0
−25
−50
−75
−100
−125
−150
−175
−200
20°N
5°N
10°S
25°S
40°S
135°W 120°W 105°W 90°W 75°W 60°W
20.00 21.00 22.00 23.00 0.00 1.00
21.00 22.00 23.00 0.00 1.00 2.00
22.00 23.00 0.00 1.00 2.00 3.00
23.00 0.00 1.00 2.00 3.00 4.00
0.00 1.00 2.00 3.00 4.00 5.00
Longitude, LT(hr)

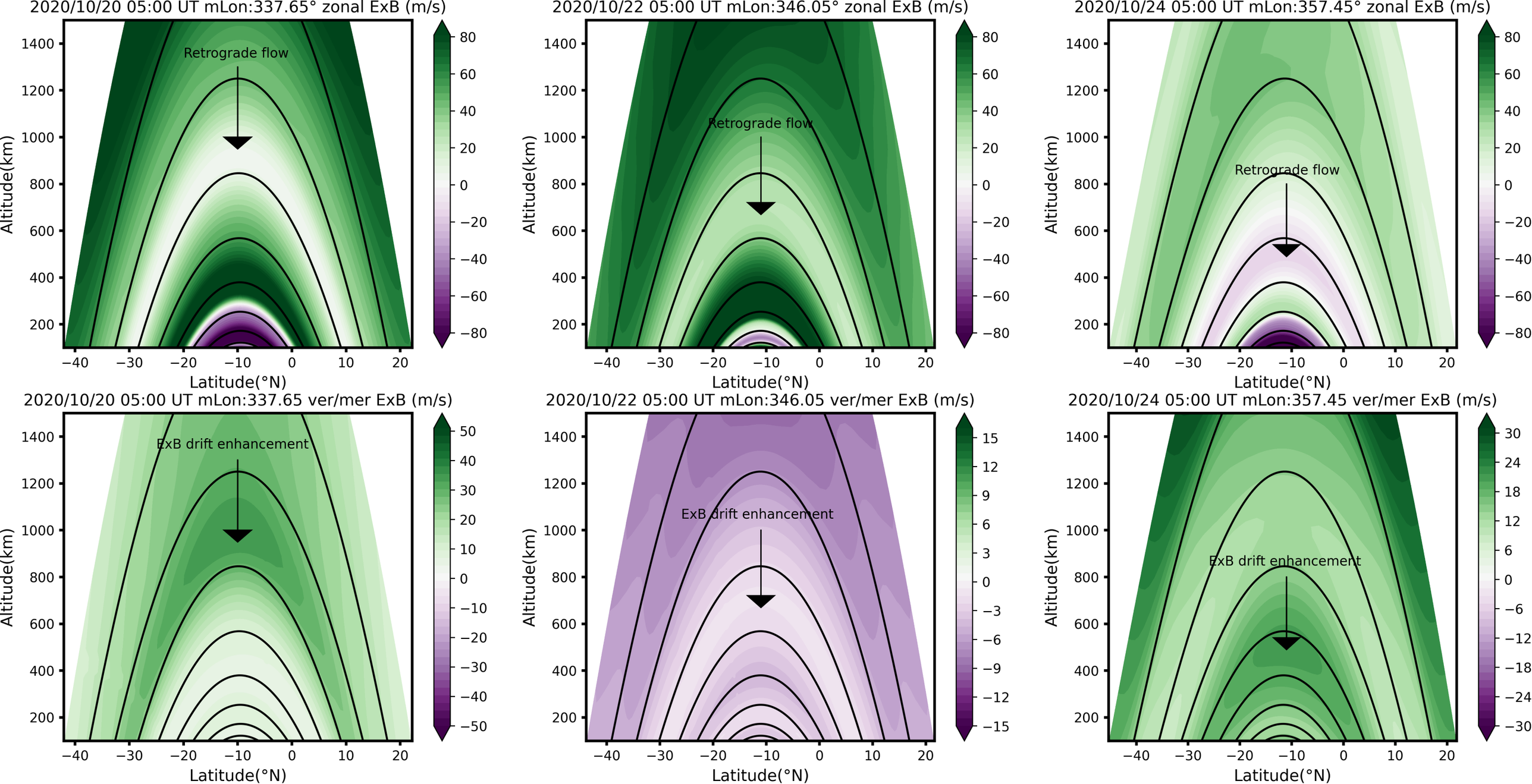
2020/10/20 05:00 UT mLon:337.65° zonal ExB (m/s)
Retrograde flow
2020/10/22 05:00 UT mLon:346.05° zonal ExB (m/s)
Retrograde flow
2020/10/24 05:00 UT mLon:357.45° zonal ExB (m/s)
Retrograde flow
2020/10/20 05:00 UT mLon:337.65 ver/mer ExB (m/s)
ExB drift enhancement
2020/10/22 05:00 UT mLon:346.05 ver/mer ExB (m/s)
ExB drift enhancement
2020/10/24 05:00 UT mLon:357.45 ver/mer ExB (m/s)
ExB drift enhancement
Altitude(km)
Latitude(°N)

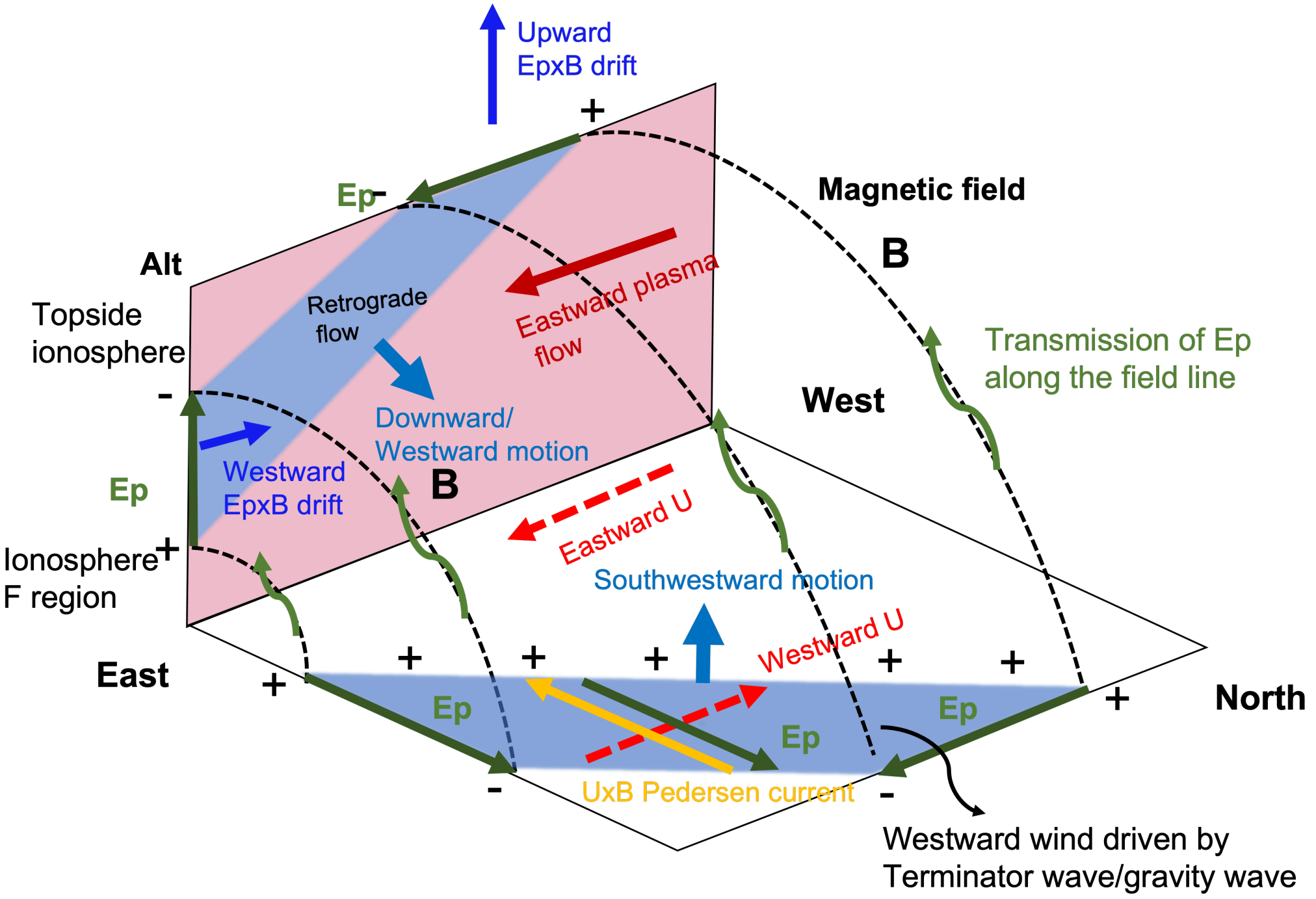
Upward
EpxB drift
+
Ep
–
Magnetic field
B
Alt
Topside
ionosphere
Retrograde
flow
Eastward plasma
flow
Transmission of Ep
along the field line
West
-
Downward/
Westward motion
Ep
Westward
EpxB drift
B
Eastward U
+
Ionosphere
F region
Southwestward motion
Westward U
East
+
+
+
+
+
+
+
Ep
Ep
Ep
North
UxB Pedersen current
-
-
Westward wind driven by
Terminator wave/gravity wave

Gravity waves seed upwellings

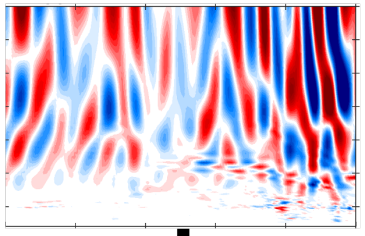

Midnight vertical ExB drift enhancement

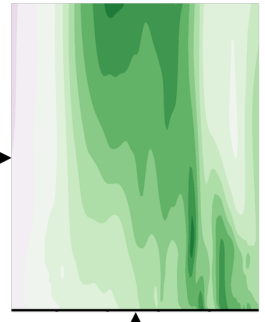

Uplift of the bottomside Ionopsheric layer

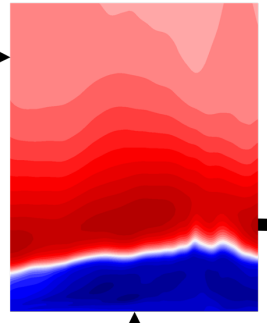

Development of Ep within upwellings

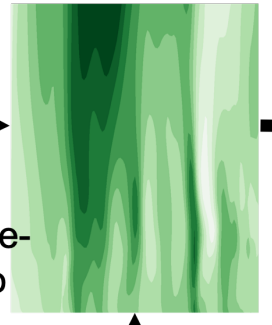

EpxB

Upwelling growth (~50 km)

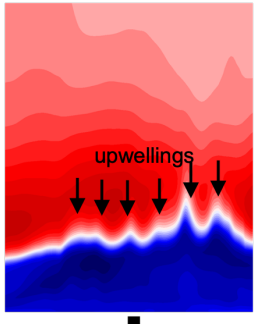

Neutral wind perturbations associated with gravity waves and solar terminator waves

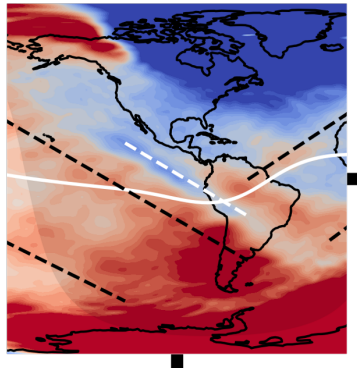

Wind-driven Ep mapping to the equatorial ionosphere

(conjugate effect)

Midnight vortex

gxB driven large-scale Ep due to large zonal Ne gradient

Destabilizing effect

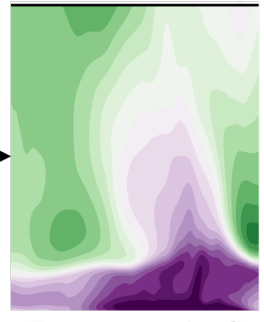

Retrograde flow (westward) of zonal ExB drift

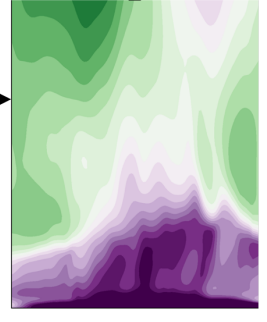

Shear flow instability

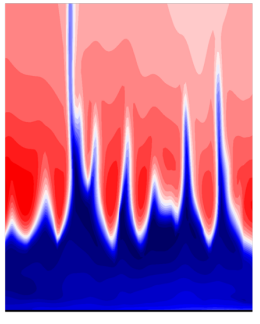

EPB development

Converging and diverging wind associated with solar terminator waves and MTM affect the ionospheric layer height

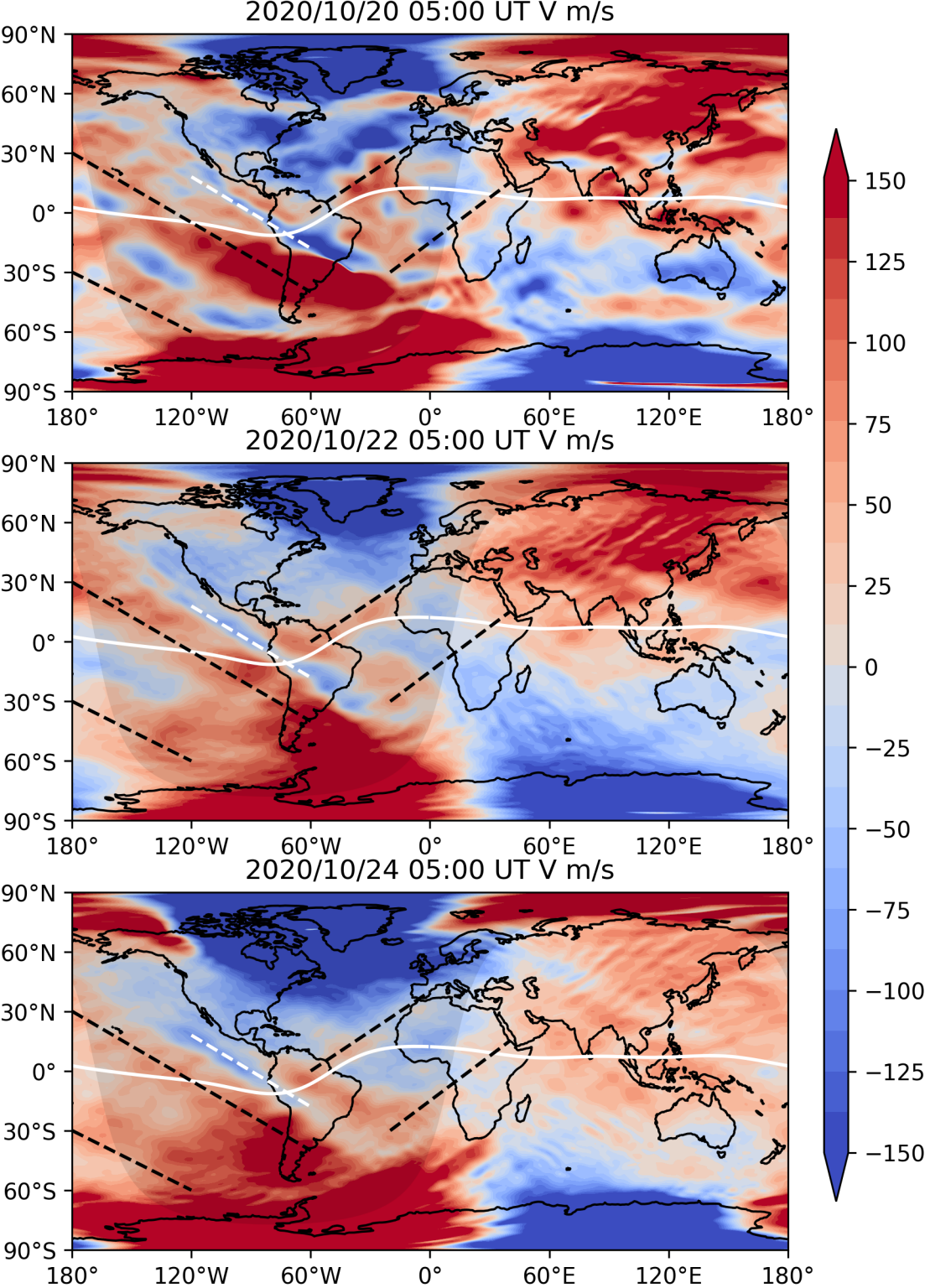
2020/10/20 05:00 UT V m/s
2020/10/22 05:00 UT V m/s
2020/10/24 05:00 UT V m/s
90°N
60°N
30°N
0°
30°S
60°S
90°S
180°
120°W
60°W
0°
60°E
120°E
180°
150
125
100
75
50
25
0
−25
−50
−75
−100
−125
−150